The tensile strength of volcanic rocks: Experiments and models

Michael J Heap, Fabian B Wadsworth, Zhen Heng, Tao Xu, Luke Griffiths, Andrea Aguilar Velasco, Emma Vairé, Marie Vistour, Valentin R Troll, Frances M Deegan, et al.

The tensile strength of volcanic rocks: Experiments and models

Michael J. Heap[1,2]*, Fabian B. Wadsworth[3], Zhen Heng[4], Tao Xu[4], Luke Griffiths[5], Andrea Aguilar Velasco[1], Emma Vairé[1], Marie Vistour[1], Thierry Reuschlé[1], Valentin R. Troll[6], Frances M. Deegan[6], and Chun'an Tang[7,8]

[1]*Université de Strasbourg, CNRS, Institut Terre et Environnement de Strasbourg, UMR 7063, 5 rue René Descartes, Strasbourg F-67084, France*

[2]*Institut Universitaire de France (IUF), 1 rue Descartes, Paris 75231, France*

[3]*Earth Science, Durham University, Science Labs, Durham, DL1 3LE, United Kingdom*

[4]*Center for Rock Instability and Seismicity Research, Northeastern University, Shenyang 110819, China*

[5]*NGI – Norwegian Geotechnical Institute, Oslo, 0806, Norway*

[6]*Department of Earth Sciences, Natural Resources and Sustainable Development (NRHU), Uppsala University, Uppsala, Sweden*

[7]*State Key Laboratory of Coastal & Offshore Engineering, Dalian University of Technology, Dalian, 116024, China*

[8]*State Key Laboratory of Geological Processes and Mineral Resources, China University of Geosciences (Wuhan), Wuhan, 430074, China*

*Corresponding author: Michael Heap (heap@unistra.fr)

Abstract

The tensile strength of volcanic rock exerts control over several key volcanic processes, including fragmentation and magma chamber rupture. Despite its importance, there is a paucity

of laboratory data for the tensile strength of volcanic rocks, leading to an incomplete understanding of the influence of microstructural parameters, such as pore size and shape (factors that vary widely for volcanic rocks), on their tensile strength. To circumvent problems associated with the variability of natural samples, we provide here a systematic study in which we use elastic damage mechanics code "Rock Failure Process Analysis" to perform numerical experiments to better understand the influence of porosity, pore diameter, pore aspect ratio, and pore orientation on the tensile strength of volcanic rocks. We find that porosity and pore diameter exert a first-order control on the tensile strength of volcanic rocks, and that pore aspect ratio and orientation also influence tensile strength. Tensile strength is reduced by up to a factor of two as porosity is increased from 0.05 to 0.35 or as pore diameter is increased from 1 to 2 mm. Small, but systematic, reductions in tensile strength are observed as the angle between the loading direction and the major axis of an elliptical pore is increased from 0 to 90°. The influence of pore aspect ratio (the ratio of the minor to major axis of an ellipse) depends on the pore angle: when the pore angle is 0°, a decrease in pore aspect ratio, from 1 (a circle) to 0.2, increases the tensile strength, whereas the same decrease in pore aspect ratio does not substantially change the tensile strength when the pore angle is 90°. These latter numerical experiments show that the tensile strength of volcanic rocks can be anisotropic. Our numerical data are in broad agreement with new and compiled experimental data for the tensile strength of volcanic rocks. One of the goals of this contribution is to provide better constrained constitutive models for the tensile strength of volcanic rocks for use in volcano modelling. To this end, we present a series of theoretical and semi-empirical constitutive models that can be used to determine the tensile strength of volcanic rocks, and highlight how tensile strength estimations can influence predictions of magma overpressures and assessments of the volume and radius of a magma chamber.

Key words: Tensile strength; volcanic rock; porosity; pore geometry; constitutive models

1 Introduction

Volcanoes and volcanic rocks are pervasively fractured at a variety of scales, and the abundance of tensile (opening-mode) fractures observed in volcanic systems speaks to the importance of the tensile strength of volcanic rocks. For example, thermal stresses can create tensile fractures on the microscale (e.g., Browning et al., 2016; Daoud et al., 2020) and the macroscale (e.g., Aydin and DeGraff, 1988; Lamur et al., 2018), the shearing of magma can create en échelon tensile fractures (e.g., Kushnir et al., 2017), and pressurised pore fluids can create hydrofractures and tuffisites (e.g., Heiken et al., 1988; Tuffen et al., 2003; Heap et al., 2019a).

The tensile strength of volcanic rocks is an important input parameter for volcano modelling (e.g., see discussion in Heap and Violay, 2021). For example, magma pressures must exceed the tensile strength of the host rock in order to propagate dykes to feed eruptions (e.g., Gudmundsson, 2006) and, therefore, the tensile strength of volcanic rocks is an important parameter in eruption forecasting (e.g., Gudmundsson, 2006; Browning et al., 2015; Zhan and Gregg, 2019). The tensile strength of volcanic rocks is also required in some volcano deformation models (e.g., Holohan et al., 2011) and as an input parameter in some discrete element method (DEM) models designed to understand dome growth and behaviour (e.g., Harnett et al., 2018; Walter et al., 2019). Finally, tensile strength also controls the fragmentation of volcanic rocks and magmas (e.g., Alidibirov, 1994; Spieler et al., 2004; Koyaguchi et al., 2008).

Experimental studies have shown that the tensile strength of volcanic rocks decreases as a function of porosity (e.g., Heap et al., 2012; Lamb et al., 2017; Hornby et al., 2019; Harnett et al., 2019; Kendrick et al., 2021; Heap and Violay, 2021). For example, Harnett et al. (2019)

found that the tensile strength of andesites from Soufrière Hills volcano (Montserrat) was reduced from ~4 to ~0.5 MPa as porosity increased from ~0.22 to ~0.4. The tensile strength of dacite from Mt Unzen volcano was reduced from ~5.75 MPa at a porosity of ~0.03 to ~1.8 MPa at a porosity of ~0.35 (Hornby et al., 2019; Kendrick et al., 2021). However, although studies have shown that pore size, shape, and orientation influence the compressive strength of volcanic rock (e.g., Heap et al., 2014a; Bubeck et al., 2016; Griffiths et al., 2017), systematic studies on the influence of these microstructural attributes on the tensile strength of volcanic rocks are currently unavailable. Understanding the effect of pore size, pore shape, and pore orientation on the tensile strength of volcanic rocks is important due to (1) the above-outlined importance of tensile strength for volcanic systems and modelling, (2) the tremendous diversity of pore geometry observed in volcanic rocks, which can also be characterised by a preferred pore shape orientation (anisotropy) (e.g., Wright et al., 2009; Shea et al., 2010; Voltolini et al., 2011), and (3) the large influence these parameters exert on the compressive strength of volcanic rocks (Heap et al., 2014a; Bubeck et al., 2016; Griffiths et al., 2017).

We present here a study in which we systematically explore the influence of porosity, pore size, pore aspect ratio, and pore orientation on the tensile strength of volcanic rocks. We performed numerical experiments to circumvent the problems associated with natural sample-to-sample variability, and the difficulty in finding suites of volcanic rocks in which only one microstructural parameter varies whilst the others remain constant. These numerical experiments, based on elastic damage mechanics, allow us to vary one parameter at a time and therefore investigate the influence of each parameter in isolation. We then compare the results of these numerical experiments with laboratory data (both unique to this study and compiled from the literature). Finally, we present a series of theoretical and semi-empirical constitutive models that can be used to estimate the tensile strength of volcanic rocks. We then outline the relevance of our results for volcano modelling. Although the input parameters for our numerical

experiments are calibrated for volcanic rocks, we highlight that the salient conclusions of this study are likely relevant for a wide range of rock types, not just volcanic rocks.

2 Materials and methods

2.1 Numerical samples and experiments

The numerical samples were generated using a 2D version of a "hard-sphere" algorithm in which circles or ellipses ("pores") are randomly generated in an aperiodic 2D domain ("groundmass"), with the requirement of no-overlap with each other. This algorithm was implemented in Python™. The numerical samples are circular bitmap images that are 375 pixels in diameter. At a resolution of 7.5 pixels/mm, the circular samples are 50 mm in diameter (the assignment of a resolution is discussed below). Three sets of samples were generated in which varied combinations of porosity, ϕ, pore radius (for circular pores), r, pore orientation, θ, and pore aspect ratio (for elliptical pores), r_a/r_b, where r_a and r_b are the minor to major semi axis of an ellipse, respectively (Table 1).

(1) Samples containing circular pores (aspect ratio of 1) were generated to contain porosities, ϕ, of 0.02, 0.05, 0.1, 0.15, 0.2, 0.25, 0.3, and 0.35, with a pore diameter, $2r$, of either 1, 1.5, or 2 mm. Two samples were generated for each combination of porosity and pore size, resulting in a total of 48 samples (Table 1).

(2) Samples containing a porosity, ϕ, of 0.1 and a pore aspect ratio, r_a/r_b, of 0.5 were generated such that their pore angles (the angle between the loading direction and the major axis of the elliptical pore), θ, were 0, 10, 20, 30, 40, 50, 60, 70, 80, and 90°. The major semi axis, r_b, in these samples was fixed at 1 mm. Two samples were generated for each angle, resulting in a total of 20 samples (Table 1).

(3) Samples containing a porosity, ϕ, of 0.1 were generated with pore angles, θ, of 0, 45, or 90° and pore aspect ratios, r_a/r_b, of 0.2, 0.25, 0.33, 0.5, and 0.67 (for a fixed

126 r_b of 1 mm). Two samples were generated for each combination of pore angle and
127 pore aspect ratio, resulting in a total of 30 samples (Table 1).
128 We generated a total of 98 numerical samples, examples of which are shown in Figure 1.
129 Although our numerical samples greatly simplify the microstructural complexity of natural
130 volcanic rocks, in simplifying the microstructure of our numerical samples (pores that are either
131 circles or ellipses) we are able to better understand the influence of individual microstructural
132 parameters on tensile strength. We can also calculate the pore number density, N, for each of
133 our numerical samples, where $N = \phi/[(1 - \phi)A_i]$. A_i represents the area of one of the pores
134 in the domain so that $A_i = \pi r_a r_b$, where $r_a = r_b \equiv r$ for circular pores. Therefore, across our
135 numerical experiments, we cover $6.50 \times 10^3 \leq N \leq 6.86 \times 10^5$ m^{-2}. We note that in our system,
136 N is an areal number density, a 2D equivalent to the 3D volumetric number density. We find
137 that, for our numerical samples, N increases and decreases as porosity and pore diameter
138 increase, respectively. We note that the pore diameters used in the numerical experiments (1–2
139 mm; Table 1) are larger than the pore diameters observed in the experimental samples (see
140 Section 2.2 below). The minimum size of a circular pore is a function of the pixel or element
141 size (the resolution of our numerical samples is 7.5 pixels/mm). Pore sizes of 1–2 mm allowed
142 us to prepare numerical samples containing not only circular pores, but also samples in which
143 we could vary the pore aspect ratio and pore angle (Table 1).
144

Porosity	**Pore diameter (circle), $2r$, or major axis diameter, $2r_b$ (ellipse) (mm)**	**Pore angle, θ (°)**	**Pore aspect ratio, r_a/r_b**	**Number of numerical samples**
0.1	1, 1.5, 2	-	1	48
0.1	2	0, 10, 20, 30, 40, 50, 60, 70, 80, 90	0.5	20

0.1	2	0, 45, 90	0.2, 0.25, 0.33, 0.5, 0.67	30

145

146 **Table 1.** Microstructural parameters (porosity, pore diameter, pore angle, and pore aspect
147 ratio) for the numerical samples generated for this study. Two samples were generated for
148 each combination of parameters, resulting in a total of 98 numerical samples.

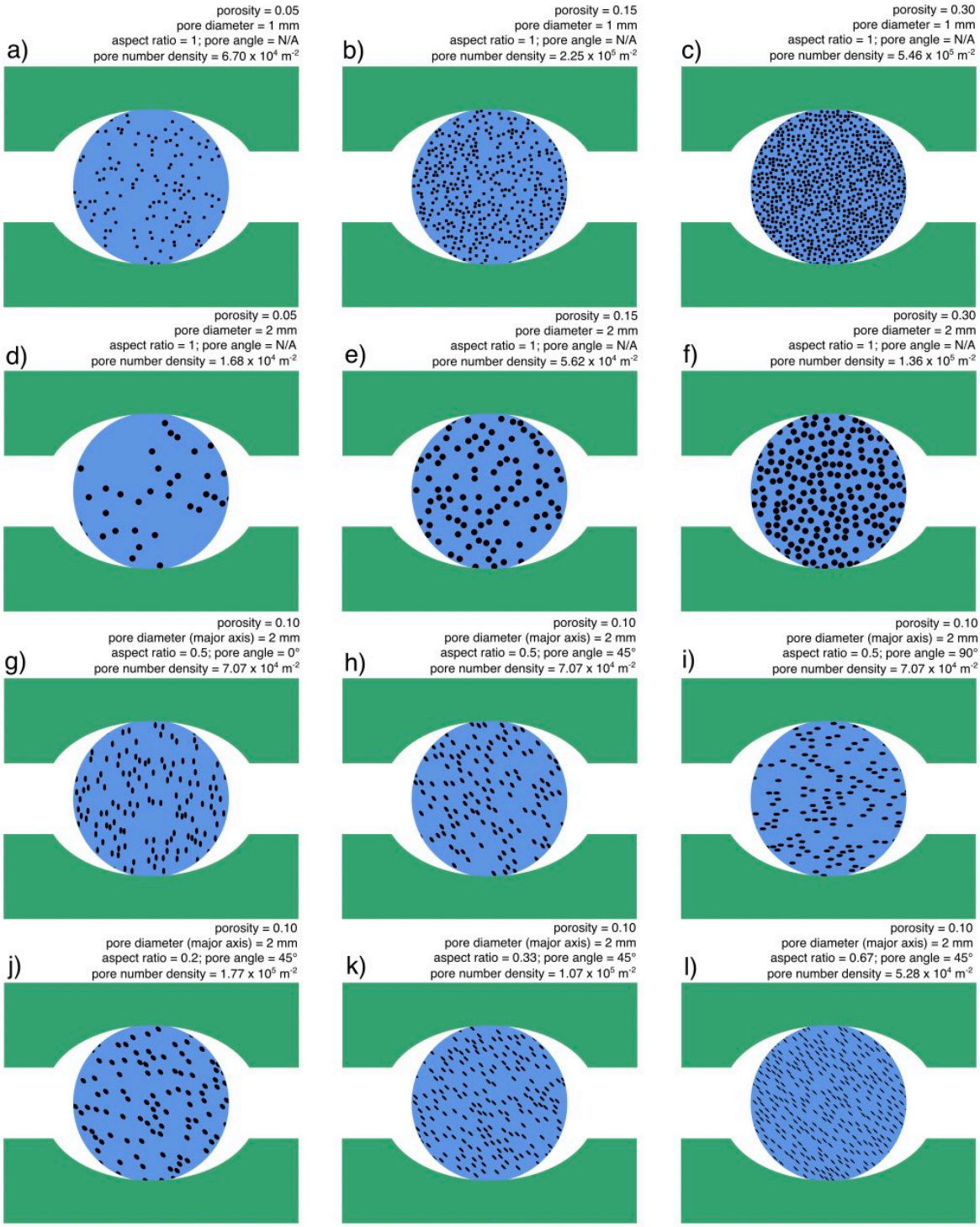

Figure 1. (a-l) Examples of the 50 mm-diameter numerical samples generated for this study. The green areas represent the loading platens typically used in laboratory experiments, the blue areas represent the solid (groundmass) sample, and the black areas represent the pores within the samples.

We then assigned physical and mechanical properties to the square pixels or elements forming the circular samples. The elements comprising the pores were assigned a very small value of Young's modulus, E_0, of 1.0×10^{-8} MPa in order to prevent the prevent the system of equations from being ill-posed and to improve numerical stability. The elements comprising the pores can deform freely, but not fail (see below). The elements representing the solid groundmass of the sample were assigned values of Young's modulus, E_0, tensile strength, σ_t, and compressive strength, σ_c, according to a Weibull probability density function (e.g., Rinne, 2008):

$$x(u) = \frac{m}{u_0}\left(\frac{u}{u_0}\right)^{m-1} exp\left[-\left(\frac{u}{u_0}\right)^{m}\right] \quad (1).$$

Where $x(u)$ is the dependence of a given property on the distribution scale input, u, such that $x(u)$ is replaced by each of $E_0\ (u)$, $\sigma_t\ (u)$, or $\sigma_c\ (u)$ in determining the probability of a certain groundmass element having a certain property. m is the Weibull shape factor or "homogeneity index" (high and low values of m will create a homogenous and heterogenous sample groundmass, respectively; see Tang et al., 2000; Xu et al., 2012), and u and u_0 are the scale parameter of an individual element and the average element value, respectively. We use values of $E_0\ (u_0)$, $\sigma_t\ (u_0)$, $\sigma_c\ (u_0)$, and m previously calibrated for volcanic rocks (Table 2; Heap et al., 2014a, 2015a, 2016; Griffiths et al., 2017).

Property	**Units**	**Value**
Homogeneity index, m	-	3
Mean uniaxial compressive strength, $\sigma_c\ (u_0)$	MPa	2300

Mean Young's modulus, E_0 (u_0)	GPa	100
Poisson's ratio	-	0.25
Ratio of compressive to tensile strength	-	10
Frictional angle (°)	°	30

176

177 **Table 2.** The average physical and mechanical properties of the elements in the generated
178 numerical samples. The same values were used in Heap et al. (2014a, 2015a, 2016) and
179 Griffiths et al. (2017).

180

181 Finally, the circular samples were deformed diametrically in compression using the 2D
182 Rock Failure Process Analysis code ($RFPA_{2D}$; Tang, 1997; Tang and Tang, 2011, 2020).
183 $RFPA_{2D}$ is a numerical code based on elastic damage mechanics that has recently been used to
184 explore the mechanical behaviour of volcanic rocks (e.g., Heap et al., 2014a, 2015a, 2016;
185 Griffiths et al., 2017). The $RFPA_{2D}$ code has also been used to perform static and dynamic
186 numerical tensile experiments on pore-free numerical samples (Zhu and Tang, 2006; Zhu et al.,
187 2012). The circular numerical samples were deformed in increments of 0.002 mm. Following
188 the first 0.002 mm increment, the stress acting on each element within the numerical sample,
189 σ, was calculated using the following linear elastic damage constitutive law:

190

191 $$\sigma = E_0(1 - D)\varepsilon \quad (2).$$

192

193 Where ε is the axial strain, E_0 is the Young's modulus of the element, and D is the isotropic
194 damage variable. If the stress acting on any one element exceeded either of the two strength
195 criteria, the Mohr-Coulomb criterion and the maximum tensile criterion, then the element was
196 damaged. The Mohr-Coulomb and maximum tensile strength criteria are defined, respectively,
197 as follows:

$$D = \begin{cases} 0, & 0 \le \varepsilon < \varepsilon_{c0} \\ 1 - \dfrac{\sigma_c}{\varepsilon E_0}, & \varepsilon_{c0} \le \varepsilon \end{cases} \quad (3),$$

$$D = \begin{cases} 0, & \varepsilon_{t0} < \varepsilon \le 0 \\ 1 - \dfrac{\sigma_t}{\varepsilon E_0}, & \varepsilon_t < \varepsilon \le \varepsilon_{t0} \\ 1, & \varepsilon \le \varepsilon_t \end{cases} \quad (4).$$

Where ε_{t0} and ε_{c0} are the critical strain in tension and compression, respectively. If an element was damaged, its Young's modulus is reduced according to the following elastic damage constitutive law:

$$E = E_0(1 - D) \quad (5).$$

If $D = 1$ for a particular element, the Young's modulus was assigned a value of 0.01 MPa to prevent the system of equations from being ill-posed. If no elements were damaged in a particular loading increment, the sample was subjected to the next 0.002 mm increment. If elements were damaged, their Young's modulus was reduced according to Equation (5), and the stress on each element was recalculated using Equation (2). If, following the recalculation of stress, the stress on any of the elements within the sample exceeded one of the strength criteria, their Young's modulus was reduced, and the stress acting on all the elements (including damaged elements) was again recalculated. The process was repeated until no new elements were damaged on a particular deformation increment. The sample was then subjected to the next 0.002 mm increment. This procedure was repeated until the sample failed macroscopically (marked by a stress drop and the formation of a throughgoing fracture). During the numerical experiments, the elements within the sample can move freely in the horizontal direction, but

221 are fixed in the vertical direction due to the position on the loading platens (as is the case for
222 tensile experiments in the laboratory, see below).
223
224 2.2 Laboratory samples and experiments
225 Cylindrical samples, 40 mm in diameter and 20 mm in length, were prepared from
226 blocks of material have been the subject of recent laboratory studies: rhyodacite from Chaos
227 Crags (Lassen Volcanic Center, USA; Ryan et al., 2020; Heap et al., 2021), trachyandesite from
228 the Chaîne des Puys near Volvic (France; Heap and Violay, 2021), andesites from Volcán de
229 Colima (Trans-Mexican Volcanic Belt, Mexico; Heap et al., 2015b; Farquharson et al., 2016,
230 2017) and Kumamoto (Japan; Farquharson et al., 2016), basaltic-andesites from Merapi
231 volcano (Sunda arc, Indonesia; Heap et al., 2019b), basalt from Mt Etna (Italy; Zhu et al., 2016),
232 and tuff from Campi Flegrei and Mt Epomeo (both Italy; Heap et al., 2014b, Marmoni et al.,
233 2017; Heap et al., 2018). Samples were prepared to a diameter of 40 mm, rather than 50 mm
234 (the diameter used for the numerical experiments), due to the small size of some of the blocks
235 of material. We do not anticipate that this reduction in diameter influenced our results.
236 Backscattered scanning electron microscope (SEM) images for all of the studied
237 materials are provided in Figure 2 (optical microscope images are provided for the two tuffs
238 from Campi Flegrei). We also determined the mean 2D equivalent pore diameter (the average
239 of the maximum and minimum Feret diameter) and pore aspect ratio (the ratio of the minor to
240 major semi axis) of the most-common macropore size from these microstructural images using
241 open-source software ImageJ (in all samples except the three tuffs, rocks for which it is difficult
242 to determine the most-common macropore size due to their heterogeneity). These data are
243 available in Table 3. Although pore size and shape vary in the studied materials (Figure 2), a
244 single value of pore diameter and pore aspect ratio for each rock is required so we can compare
245 our experimental data with the results of the numerical modelling.

The rhyodacite block from Chaos Crags (hereafter referred to as CCC) (Lassen Volcanic Center in California, USA) was sampled from the Chaos Jumbles deposit (about 2 km from the volcano summit), a cold-rock avalanche deposit resulting from the collapse of Dome C about 350 years ago (Clynne and Muffler, 2017; Ryan et al., 2020). The rhyodacite has a porphyritic texture containing phenocrysts of predominantly plagioclase and potassium feldspar within a microcrystalline groundmass (Figure 2a; Ryan et al., 2020). The mean macropore diameter and aspect ratio is 59 μm and 0.55, respectively (Table 3); microcracks are also visible in the rhyodacite from Chaos Crags (Figure 2a).

The LLB andesite block from Volcán de Colima (Trans-Mexican Volcanic Belt; Varley et al., 2019) was sampled from the La Lumbre debris-flow track on the southwestern flank of the volcano (about 6–7 km from the volcano summit) (Farquharson et al., 2017). The EZ andesite block, also from Volcán de Colima, was sampled from the El Zarco riverbed on the southeastern flank of the volcano (about 12 km from the volcano summit) (Farquharson et al., 2016). Both andesites from Volcán de Colima have a porphyritic texture consisting of predominantly plagioclase and pyroxene within a microcrystalline groundmass; both andesites also contain microcracks (Figures 2b and 2c). Although the average pore diameter is much larger in andesite LLB than EZ (204 and 22 μm, respectively), the mean pore aspect ratio is very similar (0.53 and 0.50, respectively) (Table 3). The andesite from Kumamoto (KA), from a quarry in the Kumamoto prefecture in southwest Japan, has porphyritic texture containing phenocrysts of predominantly plagioclase within a microcrystalline groundmass (Figure 2d). Kumamoto andesite has a high plagioclase content of about 50% (Nara et al., 2010a). The mean pore diameter and pore aspect ratio of Kumamoto andesite is 52 μm and 0.52, respectively (Table 3). No microcracks are observable in Kumamoto andesite (Figure 2d). The block of trachyandesite from the Chaîne des Puys (France) was sourced from a quarry Volvic (VT). The trachyandesite from Volvic has an aphanitic texture (Figure 2e) and contains pores with a mean

diameter and aspect ratio of 161 μm and 0.58, respectively (Table 3). No microcracks are observable in Volvic trachyandesite (Figure 2e).

Four blocks of basaltic-andesite were collected from the summit area of Merapi volcano (Heap et al., 2019b). These rocks are variably altered by hydrothermal processes. Block M-U is the least altered, blocks M-SA1 and MSA-2 are slightly altered, and block M-HA1 is highly altered. The most abundant alteration minerals in these basaltic-andesites are K-feldspar, K-Na-alunite, and gypsum. Blocks M-U, M-SA1, MSA-2, and M-HA1 contain 19, 9, 13, and 6 wt.% of K-feldspar, 0, 0.5, 4, and 5 wt.% of gypsum, and 0, 1, 8.5, and 11 wt.% of K-Na-alunite, respectively (Heap et al., 2019b). All four blocks are characterised by a porphyritic magmatic texture containing original phenocrysts of predominantly plagioclase and pyroxene, and secondary K-feldspar phenocrysts, within a microcrystalline groundmass (Figures 2f, 2g, 2h, and 2i; Heap et al., 2019b). Blocks M-U, M-SA1, MSA-2, and M-HA1 contain average pore diameters of 322, 180, 99, and 133 μm, respectively, and mean pore aspect ratios of 0.63, 0.49, 0.58, and 0.52, respectively (Table 3).

The basalt from Mt Etna (EB) was sourced from a quarry on the southern flank of the volcano (about 15 km from the volcano summit) (Zhu et al., 2016). The basalt from Mt Etna has an aphanitic texture (Figure 2j), with very rare plagioclase, pyroxene, and olivine phenocrysts (Zhu et al., 2016). The basalt contains pores with a mean diameter and aspect ratio of 16 μm and 0.53, respectively (Table 3), and long microcracks (which can be longer than 1 mm; Figure 2j).

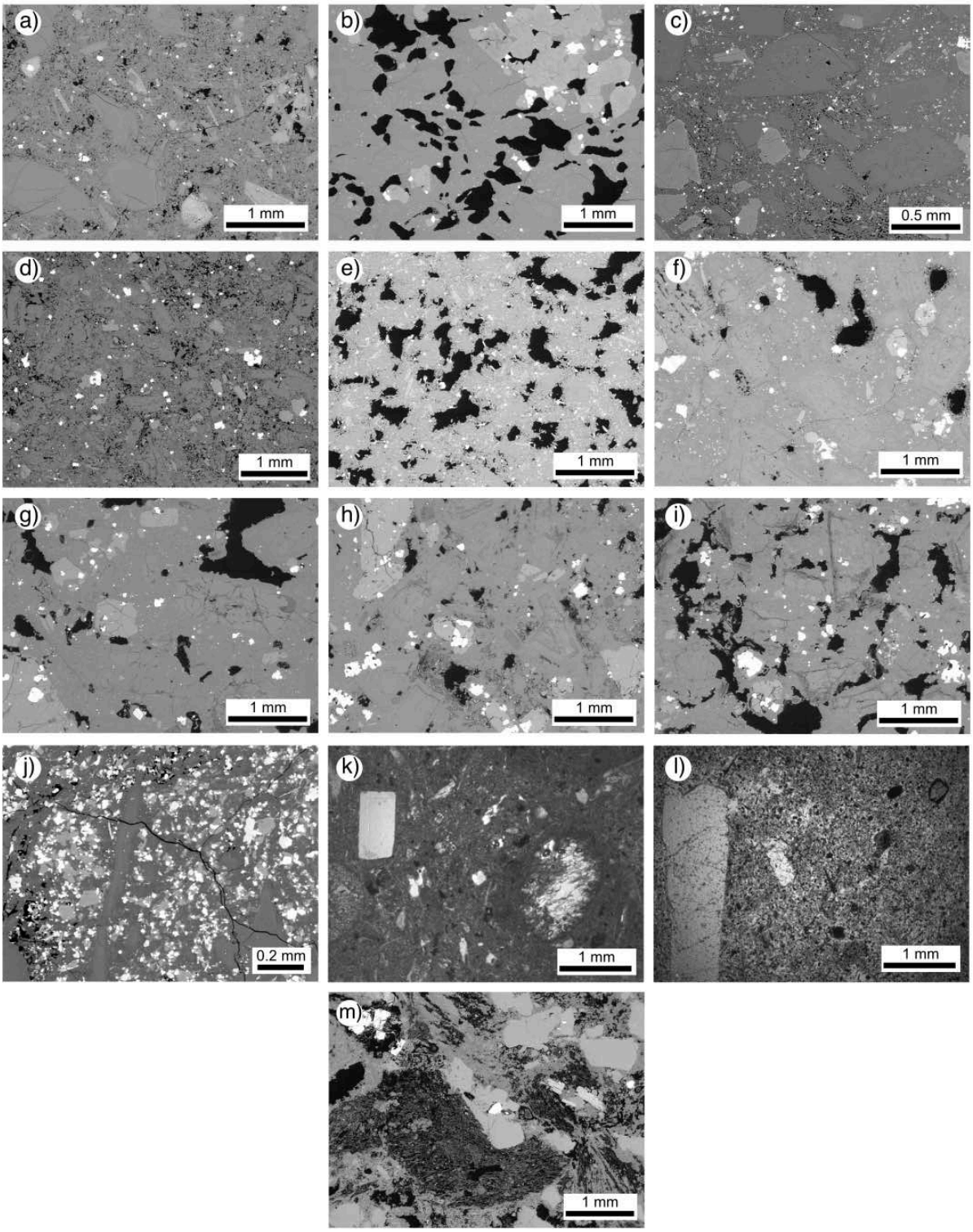

292

293 **Figure 2.** Backscattered scanning electron microscope (SEM) images of the rocks used in this

294 study (panels (k) and (l) are transmitted-light optical microscope images). (a) Dacite from

295 Chaos Crags (USA). (b) Andesite LLB from Volcán de Colima (Mexico). (c) Andesite EZ

296 from Volcán de Colima (Mexico). (d) Andesite from Kumamoto (Japan). (e) Trachyandesite

297 from Volvic (France). (f) Basaltic-andesite (M-U) from Merapi volcano (Indonesia). (g)
298 Basaltic-andesite (M-SA1) from Merapi volcano. (h) Basaltic-andesite (M-SA2) from Merapi
299 volcano. (i) Basaltic-andesite (M-HA1) from Merapi volcano. (j) Basalt from Mt Etna (Italy).
300 (k) Neapolitan Yellow Tuff from Campi Flegrei (Italy). (l) Grey Campanian Ignimbrite from
301 Campi Flegrei (Italy). (m) Mt Epomeo Green Tuff from Ischia Island (Italy). In all cases, the
302 non-black greyscale represents the crystals and groundmass and the black areas in the images
303 represent void space (pores and microcracks).
304
305 The two tuffs from Campi Flegrei are the Neapolitan Yellow Tuff (NYT), sourced from
306 an open quarry at Monte San Severino within the inferred Campi Flegrei caldera, and the Grey
307 Campanian Ignimbrite (WGI), sourced from an open quarry northwest of Caserta (Heap et al.,
308 2014b). The Mt Epomeo Green Tuff (MEGT) was collected from the flank of Mt Epomeo on
309 Ischia Island (Italy) (Marmoni et al., 2017; Heap et al., 2018). All three tuffs are texturally
310 heterogeneous pyroclastic flow deposits that contain fragments of lithics, phenocrysts, and
311 porous lapilli within a fine-grained matrix (Figures 2k, 2l, and 2m). NYT and MEGT contain
312 abundant clays and zeolites (Heap et al., 2014b, 2018), not present in WGI (Heap et al., 2014b).
313 The pore diameter and pore aspect ratio of the three tuffs are very microstructurally
314 heterogeneous and, for this reason, we consider it impossible to assign a mean pore diameter
315 and aspect ratio for these rocks.
316 The cylindrical samples prepared from these blocks were washed with water and dried
317 in a vacuum oven at 40 °C for at least 48 h. The connected porosity of each sample was
318 calculated using the bulk sample volume and the skeletal (solid) sample volume measured by a
319 helium pycnometer. The samples were then deformed diametrically by applying a vertical
320 compressive force to the loading platens at a constant stressing rate until tensile failure,
321 experiments commonly referred to as “Brazilian” tests (Bieniawski and Hawkes, 1978; Perras

and Diederichs, 2014). A schematic diagram of the experimental setup is provided as Figure 3. Axial displacement and axial load were measured using a linear variable differential transducer (LVDT) and a load cell, respectively. The displacement accumulated within the load chain was subtracted from the axial displacement. Tensile stress, σ_t, was calculated using:

$$\sigma_t = \frac{2P}{\pi dL} \quad (6),$$

where d and L are the diameter and thickness of the sample, respectively, and P is the force applied to the sample diametrically in compression. The tensile strength of the rock was taken as the tensile stress required to form the first macrofracture within the sample. All of our laboratory experiments were performed at ambient laboratory pressure and temperature.

Rock type	Pore diameter (μm)	Pore aspect ratio
Chaos Crags dacite (CCC)	59	0.55
Colima andesite (LLB)	204	0.53
Colima andesite (EZ)	22	0.50
Kumamoto andesite (KA)	52	0.52
Volvic trachyandesite (VT)	161	0.58
Merapi basaltic-andesite (M-U)	322	0.63
Merapi basaltic-andesite (M-SA1)	180	0.49
Merapi basaltic-andesite (M-SA2)	99	0.58
Merapi basaltic-andesite (M-HA1)	133	0.52
Mt Etna basalt (EB)	16	0.53

Table 3. The mean macropore equivalent diameter (the average of the maximum and minimum Feret diameter) and the average macropore aspect ratio (the ratio of the minor to major semi axis) for the studied rock types (excluding the three tuffs), determined on backscattered scanning electron microscope images (Figure 2) using ImageJ.

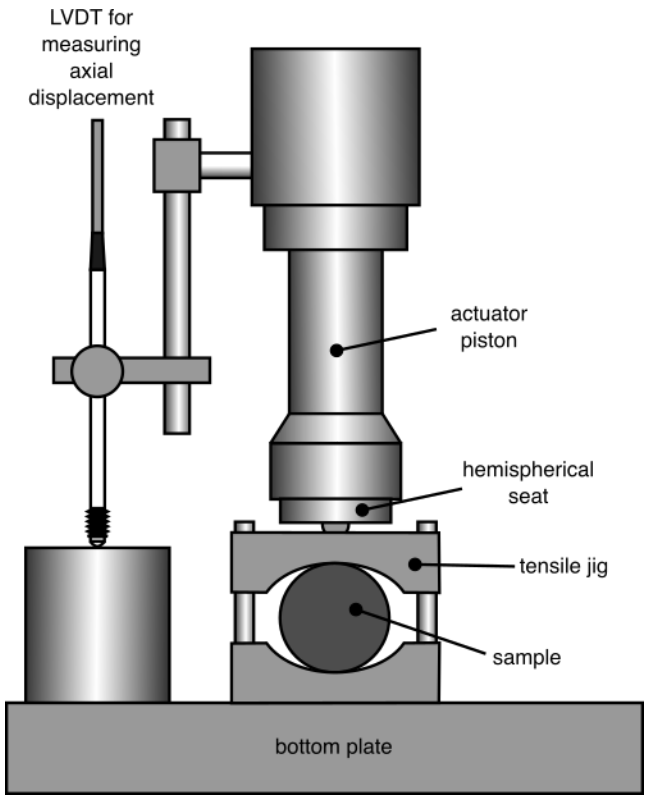

Figure 3. Schematic diagram of the laboratory setup for the indirect tensile strength experiments performed for this study. LVDT – linear variable differential transducer. Sample radius is 20 mm.

3 Results

3.1 Numerical experiments

The data from the numerical experiments are provided in Table 4. A representative force-displacement curve and snapshots of the numerical sample showing the development of the macroscopic fracture are shown in Figure 4. Macroscopic failure was signalled by a force drop, the result of the formation of a macroscopic tensile fracture (Figure 4).

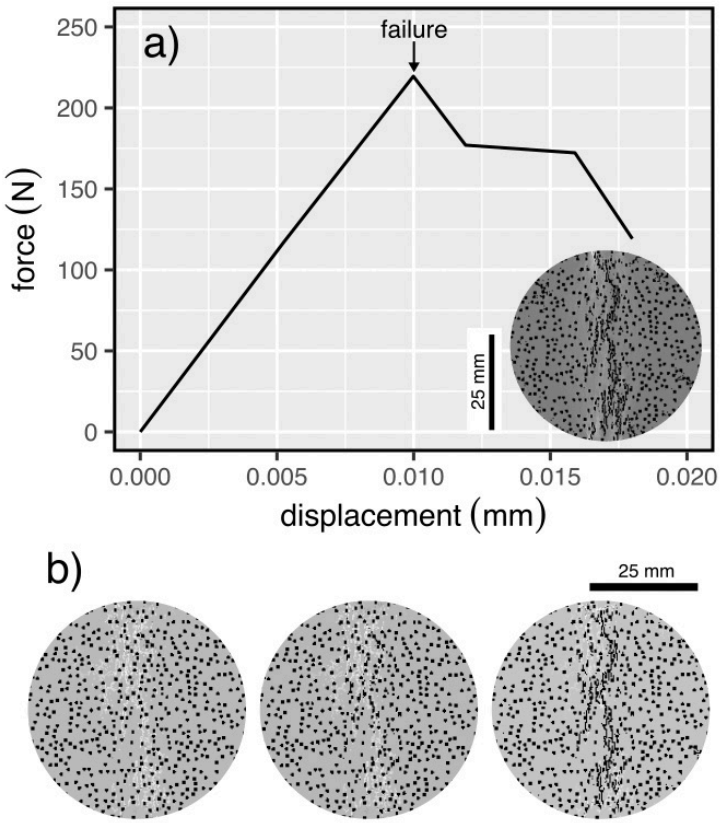

352

353 **Figure 4.** (a) Force-displacement curve for a numerical sample containing circular pores with
354 a diameter of 1 mm and a porosity of 0.3. Inset shows an image of the sample following
355 failure, showing the throughgoing tensile fracture. (b) Three snapshots of the numerical
356 sample showing the development of the macroscopic fracture (from left to right).

357

358 Figure 5 shows the results of numerical experiments designed to understand the
359 influence of pore angle on the tensile strength of volcanic rock. In these numerical experiments,
360 the porosity, pore aspect ratio, and pore diameter (the pore major axis) were fixed at 0.1, 0.5,
361 and 2 mm, respectively, and the pore angle was varied from 0 to 90°. These data show that
362 tensile strength decreases from ~2.75 MPa at an angle of 0° to ~2.5 MPa at an angle of 90°
363 (Figure 5).

364

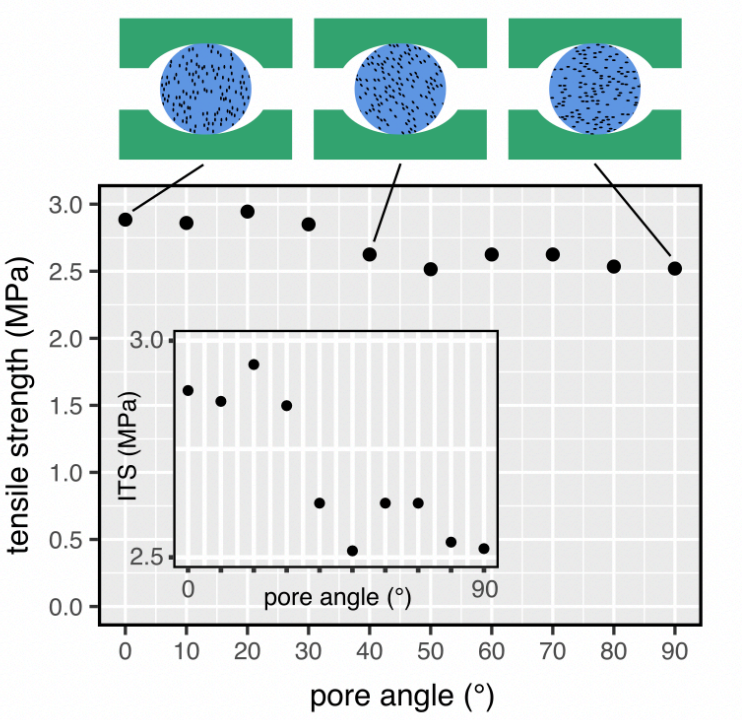

Figure 5. Indirect tensile strength as a function of pore angle from the numerical experiments. The porosity, pore aspect ratio, and pore diameter (the pore major axis) were fixed at, respectively, 0.1, 0.5, and 2 mm for these from the numerical experiments (see Table 1). Inset shows a zoom of the data. Examples of the undeformed numerical samples are provided above the graph (green – sample holder; blue – solid sample; black – porosity).

Figure 6 shows the influence of porosity and pore diameter on the tensile strength of volcanic rock. In these numerical experiments, the pore aspect ratio was 1 (the pores were circular) and the porosity was varied from 0.02 to 0.35 and the pore diameter was varied from 1 to 2 mm (Table 1). If we consider the samples with a pore diameter of 1 mm, the tensile strength was reduced from ~4.5 MPa at a porosity of 0.02 to ~2.5 MPa at a porosity of 0.35 (Figure 6). Reductions in strength as a function of porosity are of a similar magnitude when the pore diameter is 1.5 and 2 mm. Figure 6 also shows that, for a given porosity, tensile strength decreases as a function of increasing pore diameter. For example, for a porosity of 0.2, tensile strength is ~3, ~2.25, and ~1.5 MPa at pore diameters of 1, 1.5, and 2 mm, respectively. Our

results show that tensile strength decreases as pore diameter increases over the entire porosity range tested (0.02 to 0.35; Figure 6).

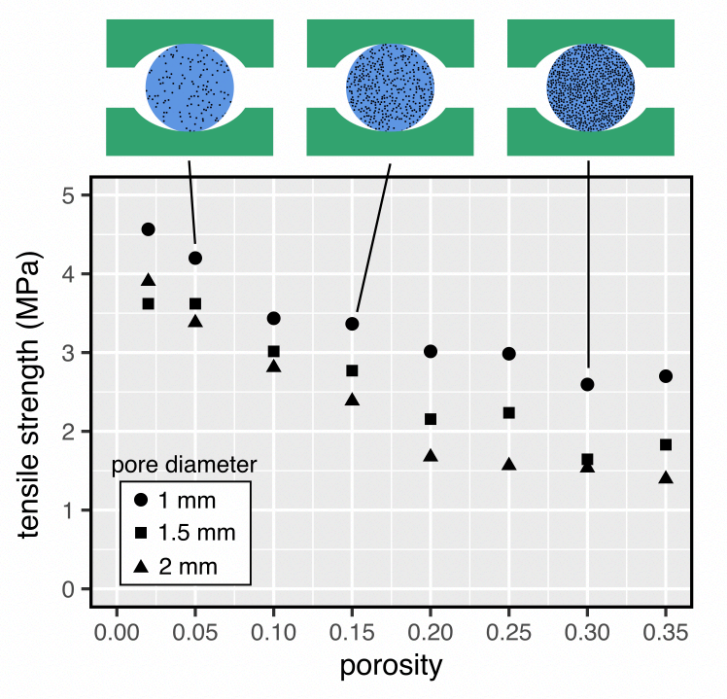

Figure 6. Indirect tensile strength as a function of porosity from the numerical experiments for three different pore diameters: 1 mm (circles), 1.5 mm (squares), and 2 mm (triangles). The pore aspect ratio was fixed at 1 (i.e. circular pores) for these from the numerical experiments (Table 1). Examples of the undeformed numerical samples are provided above the graph (green – sample holder; blue – solid sample; black – porosity).

Figure 7 shows the influence of pore aspect ratio on the tensile strength of volcanic rock. In these numerical experiments, the porosity and the maximum pore diameter (the pore major axis) were fixed at 0.1 and 2 mm, respectively, and the pore aspect ratio was varied from 0.2 to 0.67 and the pore angle was varied from 0 to 90°. Figure 7 shows that the influence of pore aspect ratio depends on the pore angle. When the pore angle is 0°, a decrease in pore aspect ratio increases the tensile strength from ~2.75 MPa at a pore aspect ratio of 1 to ~4.5 MPa at a

pore aspect ratio of 0.2. When the pore angle is 90°, a decrease in pore aspect ratio does not significantly change the tensile strength: strength is reduced from ~2.75 MPa at a pore aspect ratio of 1 to ~2.5 MPa at a pore aspect ratio of 0.2.

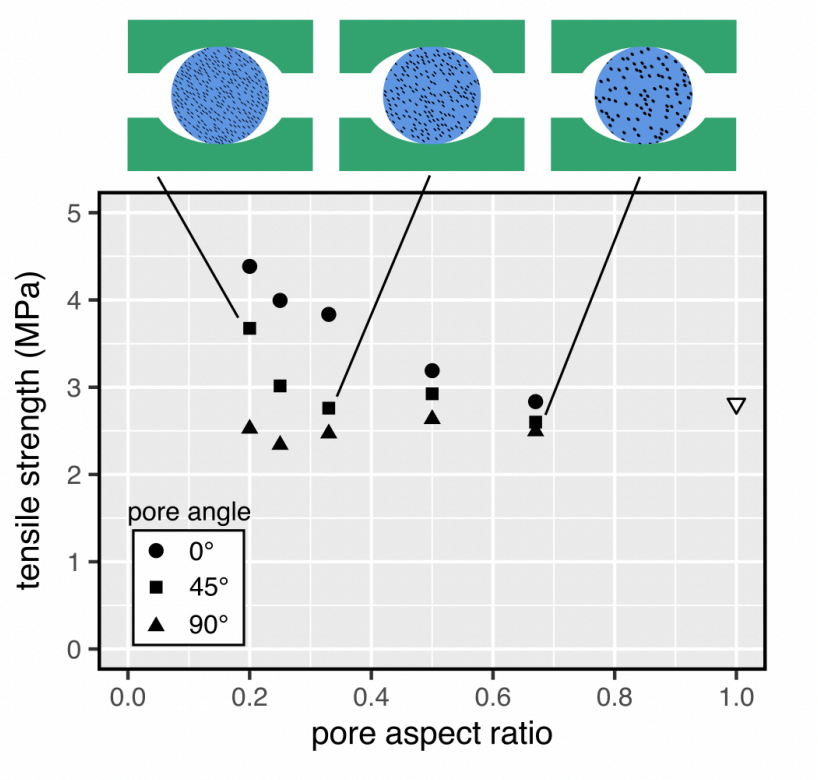

Figure 7. Indirect tensile strength as a function of pore aspect ratio from the numerical experiments for three different pore angles to the applied load: 0° (filled circles), 45° (filled squares), and 90° (filled triangles). The porosity and maximum pore diameter (the pore major axis) were fixed at, respectively, 0.1 and 2 mm for these numerical experiments (Table 1). Examples of the undeformed numerical samples are provided above the graph (green – sample holder; blue – solid sample; black – porosity).

Porosity	**Pore diameter (circle), $2r$, or major axis diameter, $2r_b$ (ellipse)**	**Pore angle (°)**	**Pore aspect ratio**	**Indirect tensile strength (MPa)**

	(mm)			
0.1	2	0	0.5	2.89
0.1	2	10	0.5	2.86
0.1	2	20	0.5	2.95
0.1	2	30	0.5	2.85
0.1	2	40	0.5	2.63
0.1	2	50	0.5	2.52
0.1	2	60	0.5	2.63
0.1	2	70	0.5	2.63
0.1	2	80	0.5	2.54
0.1	2	90	0.5	2.52
0.02	1	-	1	4.57
0.05	1	-	1	4.20
0.1	1	-	1	3.44
0.15	1	-	1	3.37
0.2	1	-	1	3.02
0.25	1	-	1	2.99
0.3	1	-	1	2.60
0.35	1	-	1	2.70
0.02	1.5	-	1	3.62
0.05	1.5	-	1	3.62
0.1	1.5	-	1	3.02
0.15	1.5	-	1	2.77
0.2	1.5	-	1	2.16
0.25	1.5	-	1	2.24
0.3	1.5	-	1	1.65
0.35	1.5	-	1	1.83
0.02	2	-	1	3.91
0.05	2	-	1	3.38
0.1	2	-	1	2.81
0.15	2	-	1	2.39
0.2	2	-	1	1.68
0.25	2	-	1	1.57
0.3	2	-	1	1.54
0.35	2	-	1	1.40
0.1	2	0	0.67	2.84
0.1	2	0	0.5	3.19
0.1	2	0	0.33	3.84
0.1	2	0	0.25	4.00
0.1	2	0	0.2	4.39
0.1	2	45	0.67	2.60
0.1	2	45	0.5	2.93

0.1	2	45	0.33	2.76
0.1	2	45	0.25	3.02
0.1	2	45	0.2	3.68
0.1	2	90	0.67	2.50
0.1	2	90	0.5	2.64
0.1	2	90	0.33	2.47
0.1	2	90	0.25	2.34
0.1	2	90	0.2	2.53

409

410 **Table 4.** Results of the numerical experiments. Pore angle is the angle between the loading
411 direction and the major axis of the elliptical pore. Pore aspect ratio is the ratio of the minor to
412 major semi axis of the pore (a circular pore has a pore aspect ratio of one). Indirect tensile
413 strength is an average of two numerical experiments.

414

415 3.2 Laboratory experiments

416 All of the laboratory data are provided in Table 5. Representative laboratory force-
417 displacement curves are shown in Figure 8. Macroscopic failure was signalled by a stress drop,
418 the result of the formation of a throughgoing tensile fracture (Figure 8). Figure 9 shows the
419 laboratory indirect tensile strengths as a function of connected porosity (Figure 9a), pore
420 diameter (Figure 9b), and pore aspect ratio (Figure 9c). The data show that indirect tensile
421 strength is reduced as porosity is reduced, from ~11–12 MPa at a porosity of ~0.05 to ~1–2
422 MPa at a porosity of ~0.45–0.50 (Figure 9a). The lowest porosity samples, the basalt from Mt
423 Etna, have the highest tensile strength (~11–12 MPa), and the highest porosity samples, the
424 three tuffs (from Campi Flegrei and Mt Epomeo), have the lowest tensile strength (~1–2 MPa)
425 (Figure 9a). Tensile strength does not vary systematically as a function of increasing pore
426 diameter (Figure 9b) and, because of the narrow range of pore aspect ratio (~0.5–0.6; Table 3),
427 it is difficult to assess the influence of pore aspect ratio on the tensile strength of the studied
428 volcanic rocks (Figure 9c).

429

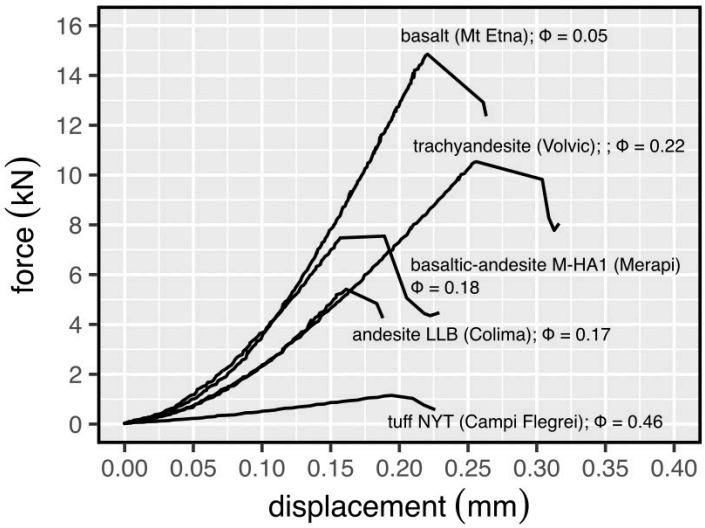

Figure 8. Representative laboratory force-displacement curves from the laboratory indirect tensile strength experiments (all data provided in Table 5).

Location	Rock type	Connected porosity	Indirect tensile strength (MPa)
Chaos Crags (USA)	rhyodacite (CCC)	0.14	5.8
Chaos Crags (USA)	rhyodacite (CCC)	0.14	5.1
Mt Etna (Italy)	basalt (EB)	0.05	11.7
Mt Etna (Italy)	basalt (EB)	0.05	11.1
Volvic (France)	trachyandesite (VT)	0.22	8.4
Volvic (France)	trachyandesite (VT)	0.22	7.9
Volcán de Colima (Mexico)	andesite (LLB)	0.16	4.3
Volcán de Colima (Mexico)	andesite (LLB)	0.17	4.2
Volcán de Colima (Mexico)	andesite (EZ)	0.09	6.5
Volcán de Colima (Mexico)	andesite (EZ)	0.08	5.9
Kumamoto (Japan)	andesite (KA)	0.13	10.1
Kumamoto (Japan)	andesite (KA)	0.14	10.1
Merapi (Indonesia)	basaltic-andesite (M-U)	0.08	7.4
Merapi (Indonesia)	basaltic-andesite (M-U)	0.09	7.0

Merapi (Indonesia)	basaltic-andesite (M-SA2)	0.09	9.7
Merapi (Indonesia)	basaltic-andesite (M-SA2)	0.09	10.1
Merapi (Indonesia)	basaltic-andesite (M-SA1)	0.22	3.0
Merapi (Indonesia)	basaltic-andesite (M-SA1)	0.25	2.1
Merapi (Indonesia)	basaltic-andesite (M-HA1)	0.18	6.0
Merapi (Indonesia)	basaltic-andesite (M-HA1)	0.21	4.6
Campi Flegrei (Italy)	tuff (NYT)	0.46	1.2
Campi Flegrei (Italy)	tuff (NYT)	0.46	0.9
Campi Flegrei (Italy)	tuff (WGI)	0.50	2.4
Campi Flegrei (Italy)	tuff (WGI)	0.50	2.1
Mt Epomeo (Italy)	tuff (MEGT)	0.44	0.9
Mt Epomeo (Italy)	tuff (MEGT)	0.46	0.8

Table 5. Results of the laboratory indirect tensile experiments performed on a selection of volcanic rocks (rhyodacite, basalt, andesite, basaltic-andesite, trachyandesite, and tuff) (see Figure 2 for microstructural images of all the studied rocks).

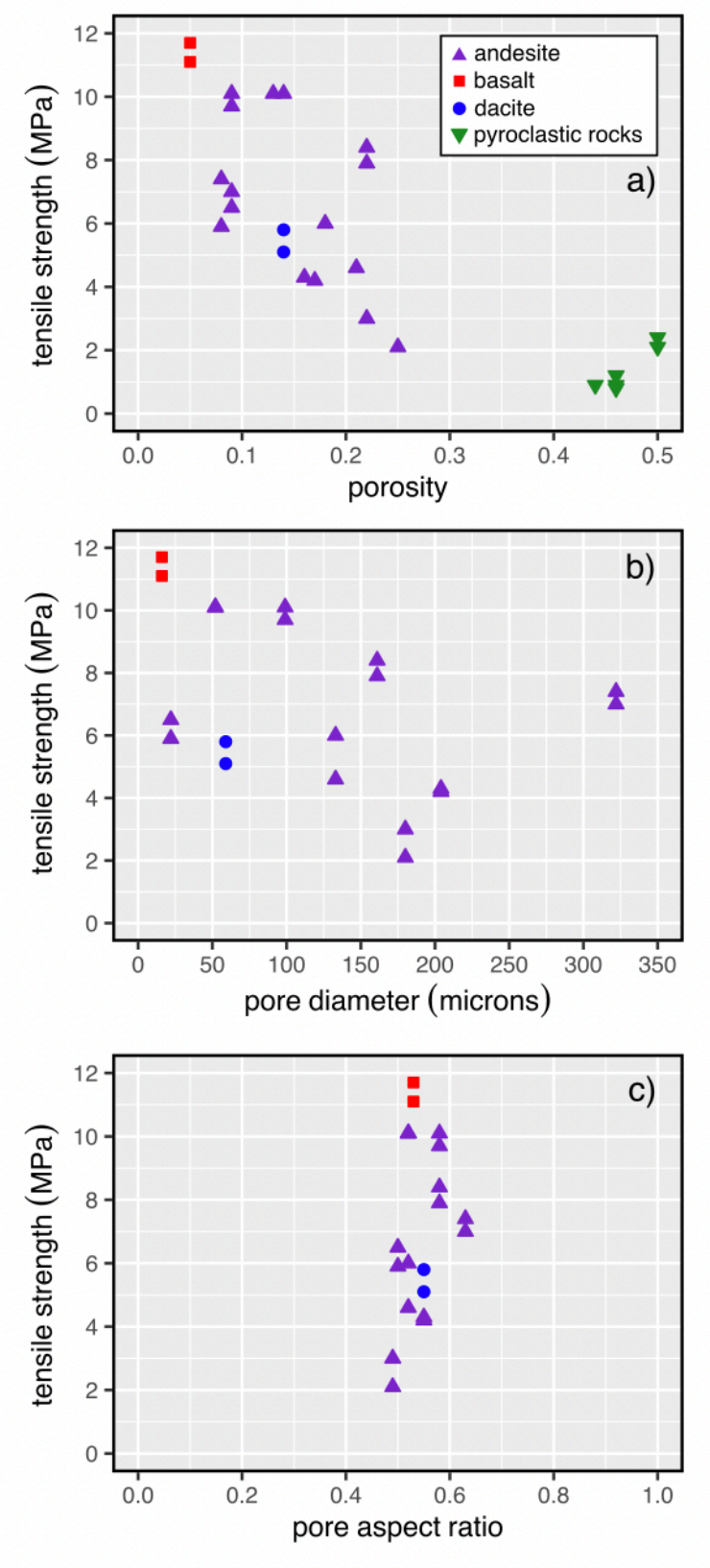

439

440 **Figure 9.** Laboratory indirect tensile strength for the volcanic rocks deformed for this study
441 as a function of (a) connected porosity, (b) average macropore diameter, and (c) average
442 macropore aspect ratio (data provided in Tables 3 and 5).

4 Discussion

The results of our numerical experiments highlight that porosity and pore geometry (pore diameter, pore aspect ratio, and pore angle) can greatly influence the tensile strength of rocks (Figures 5, 6, and 7). Our results are, therefore, in qualitative agreement with those for the compressive strength of rocks provided in Heap et al. (2014a) and Griffiths et al. (2017). For example, Heap et al. (2014a) showed that the compressive strength of volcanic rocks decreases as porosity and pore diameter increase, in accordance with the numerical tensile experiments performed for this study (Figure 6). Griffiths et al. (2017) showed, using an analytical solution for the tangential (hoop) stress along the boundary of a two-dimensional elliptical void, that the applied stress required to generate a given maximum hoop stress is higher when the pore angle is higher. These calculations explain why tensile strength decreases as a function of pore angle in our numerical experiments (Figure 5). Griffiths et al. (2017) used the same analytical solution to show that the applied stress required to maintain a given hoop stress decreases as aspect ratio decreases for high pore angles, but increases as aspect ratio decreases for low pore angles, similar to numerical data for tensile strength presented here (Figure 7). In our numerical experiments, tensile strength is not substantially influenced by aspect ratio when the pore angle is 90° (Figure 7). We highlight that the aspect ratio is varied in our numerical samples by changing the minor axis length only and so, when the pore angle is 90°, the total length of void pixels in the horizontal direction remains the same and could explain the near-constant tensile strength for the range of aspect ratios studied here (0.2–0.67).

We explored here the tensile strength of volcanic rocks containing pores. In nature, however, volcanic rocks can contain both pores and crystals (e.g., Voltolini et al., 2011). The numerical experiments presented in Heap et al. (2016) show that the presence of crystals can reduce the compressive strength of volcanic rock. It is likely, therefore, that crystals may also

serve to reduce the tensile strength of volcanic rock, offering an exciting avenue for future research.

4.2 Comparing the numerical and laboratory experiments

Figure 10a shows tensile strength decreases as a function of porosity for both the numerical (filled symbols; pore diameter from 1 to 2 mm) and laboratory experiments (open symbols; pore diameter < 1 mm; Table 3). The tensile strengths from the laboratory experiments are typically larger than those from the numerical experiments, and is likely the result of the smaller pore diameter of the laboratory samples (16–322 μm; Figure 2; Table 3) compared to the numerical samples (1–2 mm; Figure 1), a factor known to influence tensile strength (Figure 6). We also note that the pores within the numerical samples in Figure 10a are circular, which is not the case for the laboratory samples (pore aspect ratio ~0.5–0.6; Table 3). Figure 10b shows tensile strength as a function of pore aspect ratio from the numerical (filled symbols; pore angle from 0 to 90°) and laboratory experiments (open symbols; pore angle not measured). For a given pore aspect ratio, the tensile strengths from the laboratory experiments are typically larger than those from the numerical experiments (Figure 10b). Because the porosity of the laboratory samples is similar to or greater than the porosity of the numerical samples in Figure 10b (all except the basalt from Mt Etna; Table 5), the higher laboratory tensile strengths in Figure 10b is likely the result of the smaller pore diameter of the laboratory samples. The simple comparison of the results from the laboratory and numerical experiments (Figure 10) demonstrates the difficulty in studying the influence of pore geometry (pore size, pore aspect ratio, and pore angle) on the tensile strength of volcanic rocks using natural samples, highlighting the importance of the numerical experiments.

We highlight that our numerical simulations were performed in 2D and so any comparisons with laboratory experiments should be handled with care. It is known that values

493 of strength from numerical experiments are typically higher in 2D than 3D (e.g., Laghaei et al.,
494 2018). Although 3D numerical experiments, including tensile experiments, can be performed
495 using RFPA (e.g., Zhou et al., 2020; Yuan et al., 2021) they are, at present, too computational
496 expensive to perform systematic studies requiring tens or hundreds of numerical experiments.
497 Finally, we note that there is an initial non-linear part in the laboratory force-displacement
498 curves (Figure 8), typically interpreted as due to the closure of microcracks, that is not observed
499 in the numerical experiments (Figure 4). The absence of this initial non-linear portion can be
500 explained by the absence of microcracks in the numerical samples (Figure 1).
501

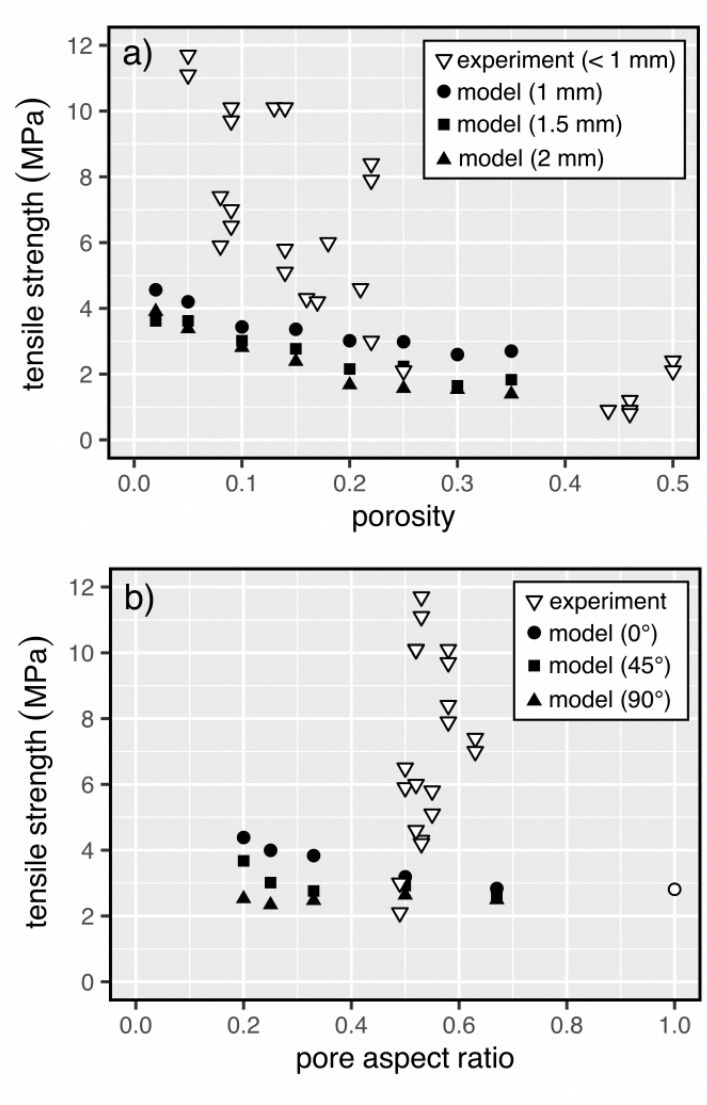

502

503 **Figure 10.** Numerical (filled symbols) and laboratory (open symbols) indirect tensile strength
504 as a function of (a) porosity and (b) pore aspect ratio. In (a), the numerical tensile strengths
505 are for three different pore diameters: 1 mm (circles), 1.5 mm (squares), and 2 mm (triangles);
506 the pore aspect ratio was fixed at 1 (i.e. circular pores) for these numerical experiments. In
507 (b), the numerical tensile strengths are for three different pore angles: 0° (circles), 45°
508 (squares), and 90° (triangles); the porosity and pore diameter (the pore major axis) were fixed
509 at, respectively, 0.1 and 2 mm for these numerical experiments.
510
511 4.2 Comparisons with previously published laboratory data
512 Our new experimental and numerical data show that tensile strength decreases non-
513 linearly as a function of increasing porosity, in accordance with compiled data from previous
514 studies on volcanic rock (Figure 11). Although our numerical data fit within the scatter of the
515 laboratory data, they typically represent the lowest tensile strength for a given porosity (Figure
516 11). The most likely explanation for the low numerical tensile strength is that the numerical
517 samples contain pores with diameters much higher (1–2 mm; Figure 1) than volcanic rocks
518 deformed in the laboratory, a microstructural variable shown to influence tensile strength
519 (Figure 6). For example, the mean macropore diameter for the samples deformed for this study
520 was 16–322 μm (Figure 2; Table 3). Other differences between the numerical samples and
521 natural samples include (1) the numerical samples have a uniform pore size (Figure 1), which
522 is not the case for natural samples (Figure 2), (2) the pores in our numerical samples are either
523 circular or elliptical (Figure 1), whereas pores in natural samples can be oddly shaped (Figure
524 2), (3) volcanic rocks typically contain microcracks (Figure 2), which are not present in the
525 numerical samples (Figure 1), and (4) all of the porosity in our numerical samples is isolated
526 (Figure 1), whereas natural volcanic rocks can contain pores that are connected by other pores,
527 pore throats, and microcracks; Figure 2).

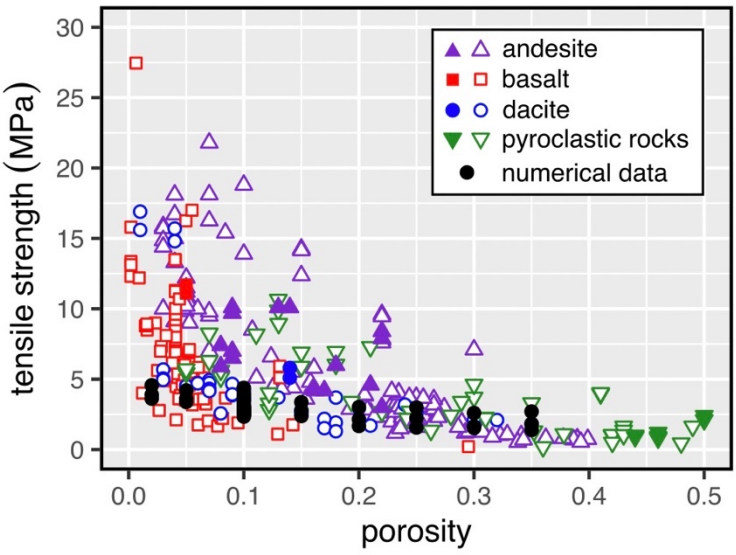

Figure 11. Tensile strength as a function of porosity for the numerical (black circles) and laboratory data (filled symbols) unique to this study, and compiled laboratory data from the literature (open symbols). Literature data from: Tuğrul and Gürpinar (1997), Gupta and Rao (2000), Chen et al. (2004), Ersoy and Atici (2007), Kılıç and Teymen (2008), Nara et al. (2010b), Kahraman and Yeken (2010), Graue et al. (2011), Lavallée et al. (2012), Heap et al. (2012), Wedekind et al. (2013), Karakuş and Akatay (2013), Hashiba and Fakui (2015), Siratovich et al. (2015), Fener and Ince (2015), Ündül and Er (2017), Yavuz et al. (2017), Lamb et al. (2017), Malik et al. (2017), Aldeeky and Hattamleh (2018), Zorn et al. (2018), Hornby et al. (2019), Harnett et al. (2019), Moon and Yang (2000), Yasar and Komurlu (2020), and Kendrick et al. (2021).

4.3 Constitutive models for tensile strength: micromechanical pore crack model

The pore-emanating crack model of Sammis and Ashby (1986), which describes an elastic medium populated with circular pores of a uniform radius, has often been employed to better understand the mechanical behaviour and failure of porous rock in compression (e.g., Baud et al., 2014), including volcanic rocks (see Heap and Violay (2021) for a review).

546 Although the pore-emanating crack model used here is the 2D empirical and analytical
547 approximation of the full solution (from Zhu et al., 2011), it has been successfully used
548 previously to glean insight on mechanical behaviour and failure of porous rock through
549 comparison with laboratory data (e.g., Baud et al., 2014). An analytical approximation for the
550 2D numerical solution of the pore crack model casts the uniaxial compressive strength, σ_c, as a
551 function of the porosity, ϕ, the fracture toughness, K_{IC}, and the pore radius, r, such that (Zhu
552 et al., 2011; Baud et al., 2014):
553
554 $$\sigma_c = \frac{1.325}{\phi^{0.414}} \frac{K_{IC}}{\sqrt{\pi r}}. \quad (7)$$
555
556 We can use this analytical approximation (Equation (7)) to better understand our tensile strength
557 data by considering the ratio of compressive to tensile strength, T, a ratio that is typically
558 between 10 and 30 for rock (Hoek and Brown, 2019). Because the $RFPA_{2D}$ model was
559 calibrated using the glass strength data from Vasseur et al. (2013) (see Table 2 and Heap et al.,
560 2014a), we use the fracture toughness of glass (K_{IC} = 0.7 MPa.m$^{0.5}$; Vasseur et al., 2013; Heap
561 and Violay, 2021) in Equation (7). Figure 12a shows that, using a σ_c/T of 15, the modelled
562 curves predicted by the pore crack model are in good agreement with the tensile strength from
563 the numerical experiments for circular pore diameters of 1, 1.5, and 2 mm. In particular, both
564 approaches predict similar increases in tensile strength as a function of decreasing pore size
565 (Figure 12a). However, the tensile strength data from the numerical experiments for non-
566 circular pores (the datapoints at a porosity of 0.1) deviate from the strength predictions from
567 the pore crack model (Figure 12b), due to the assumption of circular pores in the pore crack
568 model (Sammis and Ashby, 1986).
569

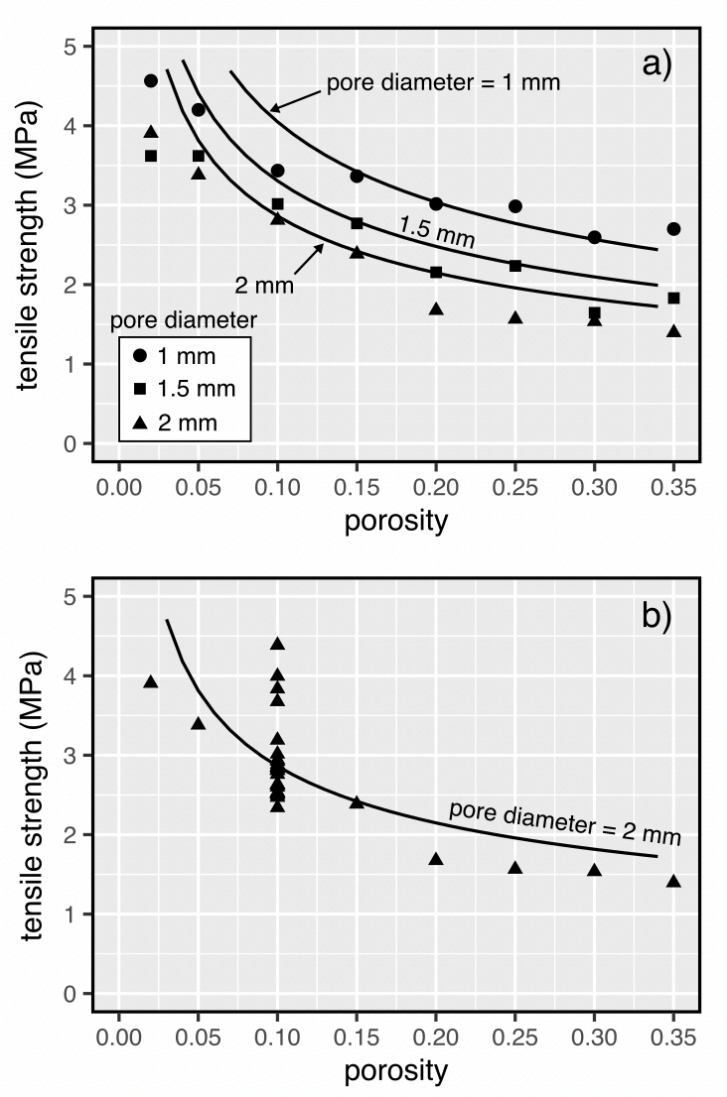

570

571 **Figure 12.** (a) Indirect tensile strength data from the numerical experiments as a function of
572 porosity for three different pore diameters: 1 mm (circles), 1.5 mm (squares), and 2 mm
573 (triangles). The pore aspect ratio was fixed at 1 (i.e. circular pores) for these numerical
574 experiments. Solid lines are modelled curves for pore diameters of 1, 1.5, and 2 mm using
575 Equation (7), assuming a fracture toughness (K_{IC}) of 0.7 MPa.m$^{0.5}$, and a ratio of tensile
576 strength to compressive of 1/15. (b) Indirect tensile strength from the numerical experiments
577 as a function of porosity for all the numerical experiments with a pore diameter of 2 mm (in
578 these numerical experiments the pore aspect ratio varies from 0.2 to 1 and the pore angle
579 varies from 0 to 90°; see Table 4). Solid line is a modelled curve for a pore diameter of 2 mm

using Equation (7), assuming a fracture toughness (K_{IC}) of 0.7 MPa.m$^{0.5}$, and a ratio of tensile strength to compressive strength of 1/15.

Although the laboratory data (data unique to this study and data compiled from the literature) are characterised by different pore diameters, pore shapes, and pore size distributions, and different values of K_{IC}, we can use Equation (7) to bracket the data for different values of $\frac{K_{IC}}{\sqrt{\pi r}}$. We find, again using a σ_c/T of 15, that the experimental data can be bracketed by curves for which $\frac{K_{IC}}{\sqrt{\pi r}}$ is equal to 4 and 80 MPa, although we note that the experimental data are better described by $\frac{K_{IC}}{\sqrt{\pi r}}$ = 17 MPa (Figure 13). By assuming values for K_{IC}, we assess the use of this model for describing the tensile strength of volcanic rocks by exploring whether the pore crack model yields reasonable pore diameter estimates for the compiled dataset. Based on the discussion provided in Heap and Violay (2021), we will assume either the fracture toughness of glass (K_{IC} = 0.7 MPa.m$^{0.5}$) or feldspar (K_{IC} = 0.3 MPa.m$^{0.5}$). When $\frac{K_{IC}}{\sqrt{\pi r}}$ is equal to 4 MPa, the value required to describe the samples with the lowest tensile strength (Figure 13), the pore diameter estimates are 3.6 and 19.4 mm for K_{IC} values of 0.3 and 0.7 MPa.m$^{0.5}$, respectively. When $\frac{K_{IC}}{\sqrt{\pi r}}$ is equal to 80 MPa, the value required to describe the samples with the highest tensile strength (Figure 13), the pore diameter estimates are 8 and 49 μm for K_{IC} values of 0.3 and 0.7 MPa.m$^{0.5}$, respectively. Although is it not unlikely that volcanic rocks can be characterised by small pore diameters (< 50 μm), the pore diameters predicted for the rocks with the lowest tensile strengths (3.6 and 19.4 mm) are clearly overestimates. One reason for this overestimate could be that the samples with the lowest tensile strengths, mostly high-porosity pyroclastic rocks, are characterised by lower values of K_{IC} (as discussed in Heap et al., 2015c). When we use a value of $\frac{K_{IC}}{\sqrt{\pi r}}$ that better describes the dataset ($\frac{K_{IC}}{\sqrt{\pi r}}$ = 17 MPa), we estimate the pore diameter

603 to be 200 μm and 1.1 mm for K_{IC} values of 0.3 and 0.7 MPa.m$^{0.5}$, respectively. The pore
604 diameter estimates for $\frac{K_{IC}}{\sqrt{\pi r}}$ = 17 MPa, which are within the range typically observed for volcanic
605 rocks measured in the laboratory (see, for example, Heap et al., 2014c), provide confidence that
606 the pore crack model (Equation (7)) can be used to estimate the tensile strength of volcanic rock
607 (using a σ_c/T of 15). The tensile strength of porous volcanic rocks can therefore be
608 approximated using the following relation:
609
610 $$T = \frac{1.325}{15\phi^{0.414}} \frac{K_{IC}}{\sqrt{\pi r}}. \quad (8)$$
611
612 Care should be taken, however, as the accuracy of tensile strength estimations using Equation
613 (8) may be low if the aspect ratio of the pores differs significantly from unity (Figure 12b).
614

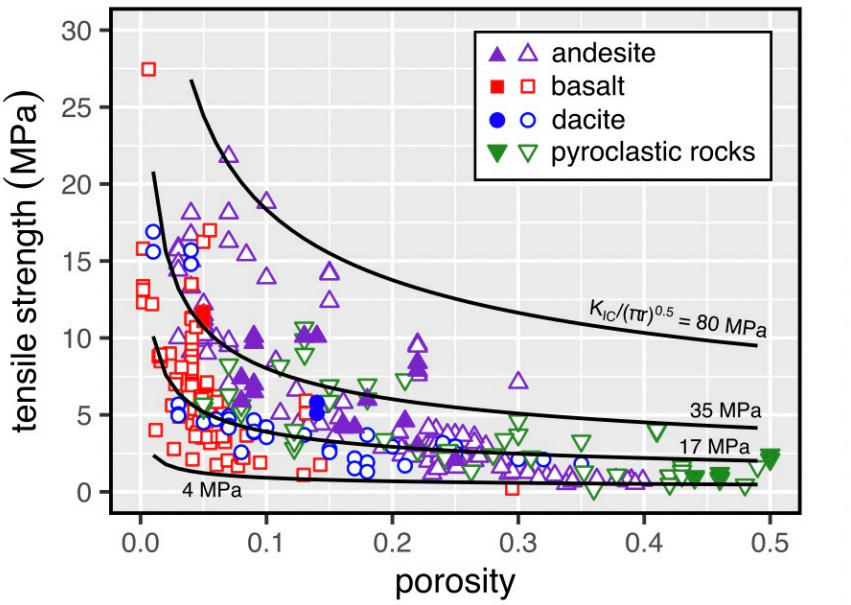

615
616 **Figure 13.** Laboratory indirect tensile strength as a function of porosity (data from this study
617 (open symbols) and compiled from the literature (filled symbols); see the caption of Figure 11

for the references). Solid lines are modelled curves for $\frac{K_{IC}}{\sqrt{\pi r}}$ = 4, 17, 35, and 80 MPa using Equation (7). See text for details.

4.4 Constitutive models for tensile strength: fragmentation models

During ascent through the crust, magma may fragment to form pyroclasts and ash particles. This fragmentation can occur via a range of dynamic processes, dominantly depending on the ascent rate of the magma and the magma material properties (Gonnermann, 2015). Generally, for magmas with a sufficiently high viscosity, η, such that viscous forces in the melt phase dominate, magma fragmentation is driven by a high bubble gas pressure relative to the magmastatic pressure (e.g., Ichihara et al., 2002), which can cause tensile rupture of the bubble walls. Rapid decompression of the magma can drive bubble gas pressure to rise, resisted by the viscosity of the melt shell, such that the overpressure can rise extremely rapidly (Spieler et al., 2004). Rapid decompression can occur due to a sudden unloading event (Manconi et al., 2009), and is extant exactly at the fragmentation interval in a rising column of magma (Degruyter et al., 2012).

Constitutive models for the critical threshold decompression, ΔP_f, have been proposed, which allow the prediction of the critical pressure drop required to rupture a bubbly magma. In most cases, the simplifying assumption is that the pressure drop and associated gas pressure rise in the bubble is sufficiently rapid that an elastic model for the melt around the bubbles is valid (e.g., Zhang, 1999; Koyaguchi et al., 2008). This is akin to assuming that the shear strain rate in the magma bubble walls induced by the bubble gas expansion is sufficiently high that a melt viscoelastic rheology is pushed to the unrelaxed elastic end-member (cf. Dingwell, 1996; Wadsworth et al., 2018). The consequence of assuming an elastic rheology for the bubble walls is that elasticity theory can be used to derive the critical pressure and rate-dependent parameters are negligible; simplifying the problem significantly.

All of the proposed theoretical or semi-empirical models take a "shell model" approach. That is, they consider the response of a single bubble in a finite elastic spherical shell to a rapid decompression, and solve for the critical pressure difference above which a fracture can propagate from the bubble wall through the shell, ΔP_f. Fragmentation is therefore considered the point when the shell breaks from edge-to-edge. McBirney and Murase (1970) proposed that ΔP_f was a function of the porosity, ϕ, via:

$$\Delta P_f = \frac{T_0(1 - 1.7\phi)^{1/2}}{\phi}, \quad (9)$$

where T_0 is an effective characteristic tensile stress. Since the model by McBirney and Murase (1970; Equation (9)), a suite of models has been proposed with similar foundations in elasticity theory, differing in the details of the assumptions made in the derivation approach. Zhang (1999) proposed that:

$$\Delta P_f = \frac{2T_0(1 - \phi)}{1 + 2\phi}. \quad (10)$$

Both Alidibirov (1994) and Koyaguchi et al. (2008) found a solution of the general form:

$$\Delta P_f = \frac{2T_0(1 - \phi^n)}{a\phi^n}, \quad (11)$$

where Alidibirov (1994) found $n = 1/3$ and $a = 1$, while Koyaguchi et al. (2008) found $n = 1$ and $a = 3$. Koyaguchi et al. (2008) additionally give a revised fragmentation criterion by taking into account the effective strength at growing crack tips:

$$\Delta P_f = \frac{2T_0(1-\phi)}{3\phi\sqrt{\phi^{-1/3}-1}}. \quad (12)$$

In the case of Equations (9) to (12), ΔP_f has a strong dependence on ϕ and is clearly dependent on the accurate determination of T_0.

Shock-tube experiments on cold or hot volcanic rocks (Spieler et al., 2004), and on silicate melts with (Martel et al., 2001) or without (Martel et al., 2000) crystalline phases have confirmed that ΔP_f is a strong function of ϕ. Empirical correlation by Spieler et al. (2004) suggested that the simplest form of this dependence of ΔP_f on ϕ was $\Delta P_c = T_0/\phi$ (note that their original correlation was simply $\Delta P \propto 1/\phi$), which matches their data reasonably well as a lower-bound. The more rigorous predictions of ΔP_f given by Equations (9) to (12) match the experimental data reasonably well, as long as T_0 is treated as a fitting parameter. In Figure 14a we show the five models given here (Equations (9) to (12) and the lower-bound $\Delta P_f = T_0/\phi$) where we take $T_0 = 1$ MPa for illustrative purposes. Koyaguchi et al. (2008) fit for T_0 using an early dataset of shock-tube fragmentation tests (Spieler et al., 2004) and found that, depending on the model used, T_0 ranged from 1.461 to 11.98 MPa.

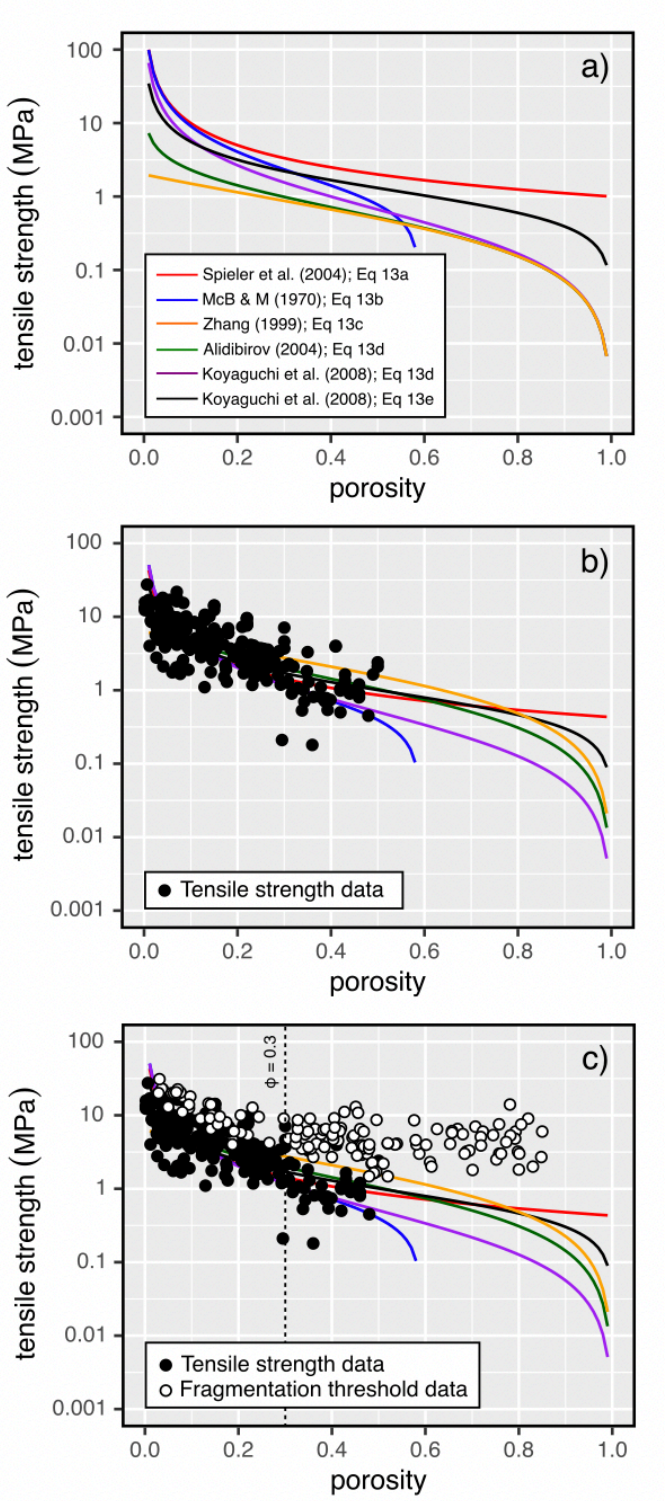

682

683 **Figure 14.** (a) Modelled tensile strength as a function of porosity using Equations (9)

684 to (12) and the Spieler et al. (2004) scaling ($\Delta P_f = T_0/\phi$), where we take T_0 = 1 MPa for

685 illustrative purposes. It is assumed here that $T \approx \Delta P_f$. (b) Modelled ensile strength as a

686 function of porosity using Equation (13), where we use the best-fit solution of Equation (13)

687 to the compiled laboratory data for the tensile strength of volcanic rocks (black circles;
688 references given in Figure 11). The best-fit values of T_0 for each equation are provided in
689 Table 6. (b) Modelled ensile strength as a function of porosity using Equation (13), where we
690 use the best-fit solution of Equation (13) to the compiled laboratory data for the tensile
691 strength (black circles; references given in Figure 11) and fragmentation threshold of volcanic
692 rocks (white circles; data from Spieler et al. (2004), Kueppers et al. (2006), Scheu et al.
693 (2006), Mueller et al. (2008), Alatorre-Ibargüengoitia et al. (2010), Kremers et al. (2010),
694 Richard et al. (2013), Mayer et al. (2015, 2016), Montanaro et al. (2016)). A line is drawn at a
695 porosity of 0.3 to indicate the porosity at which the models (i.e., Equation (13)) no longer
696 follow the fragmentation threshold data.
697
698 All of the models described above by Equations (9) to (12) and by the Spieler et al.
699 (2004) scaling $\Delta P_f = T_0/\phi$, are micromechanical models for what is a tensile bursting of an
700 array of gas-filled solid elastic shells under a given external tensile pressure. This framework
701 is therefore, conceptually akin to micromechanical models for the rupture of porous solids
702 under a tensile load (McBirney and Murase, 1970). We therefore suggest that ΔP_f could be
703 interpreted as a critical bulk tensile strength of the porous rock or magma, which accounts for
704 the stress concentration around the pores or bubbles. This is akin to saying that Equations (9)
705 to (12) and the Spieler et al. (2004) scaling can be recast as:
706
707 $$T \approx \frac{T_0}{\phi} \quad (13a)$$
708
709 $$T \approx \frac{T_0(1-1.7\phi)^{\frac{1}{2}}}{\phi} \quad (13b)$$
710

711 $$T \approx \frac{2T_0(1-\phi)}{1+2\phi} \quad (13c)$$

712

713 $$T \approx \frac{2T_0(1-\phi^n)}{a\phi^n} \quad (13d)$$

714

715 $$T \approx \frac{2T_0(1-\phi)}{3\phi\sqrt{\phi^{-1/3}-1}}. \quad (13e)$$

716

717 In Figure 14b we present the best-fit solution of Equation (13) to the compiled data for
718 $T(\phi)$ measured for volcanic rocks, and for our numerical samples for which the pores were
719 circular. The fitting is performed by allowing T_0 to vary freely, and by minimising the sum of
720 square residuals between the logarithm of the data points and the logarithm of each model result
721 at the same porosity (fit results in Table 6). We find values of T_0 that range from 0.43 to 3.14
722 MPa for the compiled tensile strength dataset, lower than those typically found when fitting for
723 fragmentation data from shock-tube experiments (T_0 ranged from 1.461 to 11.98 MPa in
724 Koyaguchi et al., 2008). Based on the good description of Equation (13) to the compiled tensile
725 strength data for volcanic rocks, we consider that Equation (13) can be used to approximate the
726 tensile strength of volcanic rocks using the values of T_0 provided in Table 6. As for Equation
727 (8) above, the accuracy of tensile strength estimations using Equation (13) may be low if the
728 aspect ratio of the pores differs significantly from unity (Figure 12b).

729

Model	**T_0 (MPa)**	**Goodness of fit**
Spieler et al. (2004) Equation (13a)	0.43	0.9948
McBirney and Murase (1970) Equation (13b)	0.51	0.9939
Zhang (1999)	3.14	0.9961

Equation (13c)		
Alidibirov (1994) Equation (13d) ($n = 1/3;\ a = 1$)	2.00	0.9970
Koyaguchi et al. (2008) Equation (13d) ($n = 1;\ a = 3$)	0.76	0.9939
Koyaguchi et al. (2008) Equation (13e)	0.77	0.9961

730

731 **Table 6.** Best-fit values for the effective characteristic tensile stress, T_0, and the associated
732 goodness of fit values, for the compiled laboratory data (see Figure 14b and 14c).

733

734 We also compile published data from shock-tube experiments for rock (cold) and
735 magma (hot) fragmentation thresholds under rapid decompression (Spieler et al., 2004;
736 Kueppers et al., 2006; Scheu et al., 2006; Mueller et al., 2008; Alatorre-Ibargüengoitia et al.,
737 2010; Kremers et al., 2010; Richard et al., 2013; Mayer et al., 2015, 2016; Montanaro et al.,
738 2016). In Figure 14c, we show these data together with compiled volcanic rock tensile strength
739 data, and the models from Equation (13) using the best-fit values of T_0 from Table 6 (where the
740 fits were performed against the compiled tensile strength data only). We note that the data from
741 shock-tube experiments approaches the data for direct tensile strength tests on volcanic rocks,
742 and the associated model fits at low porosity, but diverge at high porosity. Indeed, at high
743 porosity, the tensile strength data cluster around an apparently porosity independent value of
744 tensile strength, and the reduction in the critical decompression required to fragment the
745 samples becomes approximately constant, in contrast with the model predictions (Figure 14c).
746 Mueller et al. (2008) suggested that positive deviations from model predictions, such as shown
747 here (Figure 14c), could be the result of permeable leakage of overpressure from connected and
748 permeable pore space during decompression. This permeable leakage invalidates the model

749 predictions (Equation (13)) which are strictly based on closed pore geometries. Mueller et al.
750 (2008) provided an empirical correction to the fragmentation (or tensile strength) laws from
751 Equation (13), which captured this deviation. We find it compelling that the data from the
752 shock-tube experiments diverges strongly from the direct tensile strength test data for volcanic
753 rocks, and from the model predictions, for $\phi \gtrsim 0.2 - 0.3$. In Figure 14c, we show a vertical
754 threshold at $\phi = 0.3$, above which most volcanic rocks are considered to have a high
755 permeability (Mueller et al., 2005; Farquharson et al., 2015). It is conceivable that the shock-
756 tube experiments provide valid one-dimensional approximations to a direct tensile strength test
757 when $\phi < 0.3$, but that permeable leakage affects these measurements at $\phi > 0.3$. It is
758 therefore of first-order importance to constrain the permeability of volcanic rocks and magmas
759 to understand rock and magma fragmentation (Mueller et al., 2008). We further note that, below
760 a porosity of 0.3, laboratory measurements of tensile strength, measurements much less
761 involved than fragmentation experiments, will well approximate the fragmentation threshold of
762 volcanic rocks and magmas.
763
764 4.5 Implications for magma chamber rupture, dyking, and magma chamber volume estimates
765 The rupture of a magma chamber, allowing for dyke initiation and propagation, is
766 thought to occur when the following expression is satisfied (Gudmundsson, 2006):
767
768 $$P_1 + P_e = \sigma_3 + T, \quad (14)$$
769
770 where P_1 is the lithostatic pressure, P_e is the magma overpressure ($P_e = P_m - P_1$, where P_m is
771 the magma pressure), σ_3 is the minimum principal compressive stress, and T is the tensile
772 strength of the host rock. Estimates of magma overpressures required for magma chamber
773 rupture therefore depend on robust values of the tensile strength of the host rock. Our laboratory

and numerical data highlight that porosity and pore geometry (pore aspect ratio and pore angle) can greatly influence the tensile strength of rocks (Figures 5, 6, 7, and 9). For example, at a porosity of 0.25, tensile strength can be reduced from 3 to 1.5 MPa as the pore diameter is increased from 1 to 2 mm (Figure 6). Therefore, if possible, these factors should be considered when estimating the tensile strength of rock to provide estimates of the magma overpressure required for magma chamber rupture.

Once the magma chamber has been ruptured, the simplest condition for propagation of a dyke through the host rock is that the magma pressure, P_m, exceeds the minimum principal compressive stress, σ_3, the tensile strength of the host rock, T, and the pressure required to hold open the resultant crack of a given width, P_s (i.e. $P_m > \sigma_3 + T + P_s$). If we take the magma overpressure to be $\Delta P_m = P_m - \sigma_3$, then this dyke propagation condition is (Gudmundsson, 1983a; 1983b):

$$\Delta P_m = T + P_s = T + \frac{E}{2(1-\nu^2)}\frac{W}{L}, \quad (15)$$

for which E is the Young's modulus of the host rock, W and L are a dyke width and length, respectively, and ν is the Poisson's ratio of the host rock. Equation (15) shows that the tensile strength of the host rock through which the dyke must propagate exerts a first-order control on the overpressures required in dyke advance, and so estimates of magma overpressure rely on robust values of the tensile strength of the host rock.

Finally, the volume of a magma chamber, V_m, can be estimated using the total erupted volume, V_e, the tensile strength of the host rock, T, and the compressibility of the host rock and magma, β_r and β_m, respectively (Gudmundsson, 1987; Browning et al., 2015):

798 $$V_m = \frac{V_e}{T(\beta_m + \beta_r)}. \quad (16)$$

799

800 Taking β_r and β_m as, respectively, 3.0×10^{-11} and 1.25×10^{-10} Pa^{-1} (Gudmundsson, 1987;
801 Browning et al., 2015) and assuming values of V_e of 5×10^7, 2.5×10^8, 1×10^9 m^3 (0.05, 0.25,
802 and 1 km^3, respectively), we can investigate the influence of T on estimations of magma
803 chamber volume and, in turn, on magma chamber radius (assuming a spherical magma
804 chamber). We find that small changes in tensile strength at $T < 5$ MPa result in large changes
805 in both magma chamber volume and radius (Figure 15). At $T > 5$ MPa, small changes in tensile
806 strength result in relatively small changes in magma chamber volume and radius (Figure 15).
807 Since the majority of volcanic rocks have a tensile strength below 5 MPa (Figure 11), it is
808 therefore important to carefully consider the tensile strength used in Equation (16).

809

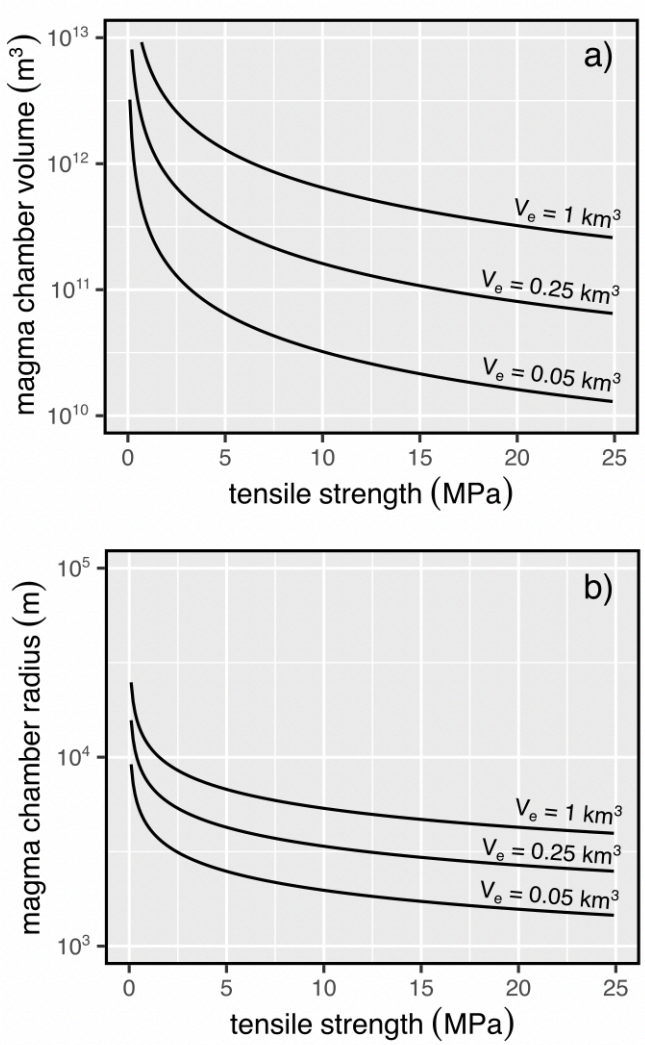

Figure 15. Magma chamber volume required to produce an eruption of a given size (a) and radius (b) as a function of host-rock tensile strength, using Equation (16). Taking β_r and β_m as, respectively, 3.0×10^{-11} and 1.25×10^{-10} Pa^{-1} and assuming values of V_e of 5×10^7, 2.5×10^8, 1×10^9 m^3 (0.05, 0.25, and 1 km^3, respectively).

In the case of Gudmundsson (1987) and Browning et al. (2015), for example, the tensile strengths used in the above equations were taken from in-situ tensile strengths from borehole measurements (e.g., Haimson and Rummel, 1982). However, in the likely case that borehole data are not available, values of tensile strength for Equations (14) to (16) will rely on (1) laboratory measurements of tensile strength performed on site-specific samples, (2) tensile

strengths estimated using the porosity of site-specific samples and Equation (13) or, if KIC and the pore radius are also known, Equation (8), and (3) values of tensile strength for the main lithology of the studied area taken from previous experimental studies (Figure 11). Alternatively, authors could use borehole data collected at other sites (e.g., Haimson and Rummel, 1982; Amadei and Stephansson, 1997). Site-specific borehole measurements could be considered the most appropriate data to use in Equations (14) to (16), as they are performed at non-zero confining pressures (i.e. at depth) and likely better represent the lengthscale of interest. Tensile strength is thought to be affected by confining pressure (e.g., Wu et al., 2016; Lan et al., 2019; Li et al., 2019) and lengthscale (e.g., Schultz, 1995; Jónsson, 2012), although more data, especially for volcanic rocks, are required to better understand their influence on tensile strength. Whatever the preferred method to measure or estimate values of tensile strength for Equations (14) to (16), we highlight that the accuracy of this value will determine the accuracy of, for example, predictions of the magma overpressures required for rupture and dyke propagation (Equations (14) and (15)) and magma volume estimates (Equation (16)). Finally, we note that not all magma chambers are located within volcanic rock. For example, the magma chamber within Cadillac Mountain in Maine (USA) was located with plutonic and sedimentary rocks (Wiebe et al., 2021), and the magma chambers of many volcanoes are thought to be located in carbonate rocks, such as Mt Etna (Heap et al., 2013; Wiesmaier et al., 2015) and Merapi volcano (Deegan et al., 2010; Troll et al., 2012). In such scenarios, modellers may want to use values of tensile strength for plutonic or sedimentary rocks, rather than the data for volcanic rocks compiled here (Figure 11). However, we consider the salient conclusions of our study, such as the influence of porosity and pore geometry, as relevant for a wide range of rock types, not just volcanic rocks.

5 Conclusions

Our numerical experiments have shown that the tensile strength of volcanic rocks, an important input parameter in a range of volcano models, depends to a first-order on porosity and pore size. Our numerical experiments have also highlighted a second-order role for pore aspect ratio and pore angle in dictating the tensile strength of volcanic rocks. These latter numerical experiments highlight that the tensile strength of volcanic rock can be anisotropic. Our numerical data are in general agreement with new and compiled laboratory data for the tensile strength of volcanic rocks. Comparison of the numerical and laboratory data highlights that, due to the natural heterogeneity and variability of natural volcanic rocks, discerning the role of pore geometry on the tensile strength of volcanic rocks using laboratory experiments alone would represent a significant challenge. Although the theoretical and semi-empirical constitutive equations provided here, i.e. Equations (8) and (13), to do not take pore aspect ratio or angle into account, parameters that we show influence tensile strength, they provide a means to estimate the tensile strength of volcanic rocks using rock physical properties that are relatively straightforward to measure in the laboratory and the field, such as porosity. These results can now help to better equip volcano modellers that require estimations of the tensile strength of volcanic rocks for their models. Although we focused here on volcanic rocks, we highlight that the salient conclusions of this study are likely relevant for a wide range of rock types, not just volcanic rocks.

Acknowledgements

We thank Bertrand Renaudié for preparing the experimental samples. T. Xu acknowledges funding from the National Natural Science Foundation of China (grant number 51974062). M. Heap acknowledges support from the Institut Universitaire de France (IUF). The authors would like to thank John Browning and Stephan Kolzenburg for constructive comments that helped improve this manuscript.

CRediT author statement

M.J. Heap – Conceptualization; Formal analysis; Investigation; Writing - Original Draft; Visualization; Supervision; Project administration; Funding acquisition

F.B. Wadsworth – Conceptualization; Formal analysis; Writing - Review & Editing

Z. Heng – Methodology; Software; Investigation

T. Xu – Methodology; Software; Investigation; Resources; Writing - Review & Editing; Supervision; Funding acquisition

L. Griffiths – Conceptualization; Methodology; Resources; Writing - Review & Editing

A. Aguilar Velasco – Investigation

E. Vairé – Investigation

M. Vistour – Investigation

T. Reuschlé – Methodology; Writing - Review & Editing

V.R. Troll – Resources; Writing - Review & Editing

F.M. Deegan – Resources; Writing - Review & Editing

C.-a. Tang – Methodology; Software; Resources; Writing - Review & Editing

References

Alatorre-Ibargüengoitia, M. A., Scheu, B., Dingwell, D. B., Delgado-Granados, H., & Taddeucci, J. (2010). Energy consumption by magmatic fragmentation and pyroclast ejection during Vulcanian eruptions. Earth and Planetary Science Letters, 291(1-4), 60-69.

Alidibirov, M. A. (1994). A model for viscous magma fragmentation during volcanic blasts. Bulletin of Volcanology, 56(6), 459-465.

Aldeeky, H., & Al Hattamleh, O. (2018). Prediction of engineering properties of basalt rock in Jordan using ultrasonic pulse velocity test. Geotechnical and Geological Engineering, 36(6), 3511-3525.

Amadei, B., & Stephansson, O. (1997). Rock stress and its measurement. Springer Science & Business Media.

Aydin, A., & DeGraff, J. M. (1988). Evolution of polygonal fracture patterns in lava flows. Science, 239(4839), 471-476.

902 Baud, P., Wong, T. F., & Zhu, W. (2014). Effects of porosity and crack density on the
903 compressive strength of rocks. International Journal of Rock Mechanics and Mining
904 Sciences, 67, 202-211.
905 Bieniawski, Z. T., & Hawkes, I. (1978). Suggested methods for determining tensile strength of
906 rock materials. International Journal of Rock Mechanics and Mining Sciences, 15(3), 99-
907 103.
908 Browning, J., Drymoni, K., & Gudmundsson, A. (2015). Forecasting magma-chamber rupture
909 at Santorini volcano, Greece. Scientific Reports, 5(1), 1-8.
910 Browning, J., Meredith, P., & Gudmundsson, A. (2016). Cooling-dominated cracking in
911 thermally stressed volcanic rocks. Geophysical Research Letters, 43(16), 8417-8425.
912 Bubeck, A., Walker, R. J., Healy, D., Dobbs, M., & Holwell, D. A. (2017). Pore geometry as a
913 control on rock strength. Earth and Planetary Science Letters, 457, 38-48.
914 Chen, T. C., Yeung, M. R., & Mori, N. (2004). Effect of water saturation on deterioration of
915 welded tuff due to freeze-thaw action. Cold Regions Science and Technology, 38(2-3),
916 127-136.
917 Clynne, M. A., & Muffler, L. P. (2017). Geologic field-trip guide to the Lassen segment of the
918 Cascades Arc, northern California (No. 2017-5022-K2). US Geological Survey.
919 Daoud, A., Browning, J., Meredith, P. G., & Mitchell, T. M. (2020). Microstructural Controls
920 on Thermal Crack Damage and the Presence of a Temperature-Memory Effect During
921 Cyclic Thermal Stressing of Rocks. Geophysical Research Letters, 47(19),
922 e2020GL088693.
923 Deegan, F. M., Troll, V. R., Freda, C., Misiti, V., Chadwick, J. P., McLeod, C. L., & Davidson,
924 J. P. (2010). Magma–carbonate interaction processes and associated CO2 release at
925 Merapi Volcano, Indonesia: insights from experimental petrology. Journal of Petrology,
926 51(5), 1027-1051.
927 Degruyter, W., Bachmann, O., Burgisser, A., & Manga, M. (2012). The effects of outgassing
928 on the transition between effusive and explosive silicic eruptions. Earth and Planetary
929 Science Letters, 349, 161-170.
930 Dingwell, D. B. (1996). Volcanic Dilemma--Flow or Blow? Science, 273(5278), 1054-1055.
931 Ersoy, A., & Atici, U. (2007). Correlation of P and S-Waves with Cutting Specific Energy and
932 Dominant Properties of Volcanic and Carbonate Rocks. Rock Mechanics and Rock
933 Engineering, 40(5), 491-504.
934 Farquharson, J., Heap, M. J., Varley, N. R., Baud, P., & Reuschlé, T. (2015). Permeability and
935 porosity relationships of edifice-forming andesites: a combined field and laboratory
936 study. Journal of Volcanology and Geothermal Research, 297, 52-68.
937 Farquharson, J. I., Heap, M. J., & Baud, P. (2016). Strain-induced permeability increase in
938 volcanic rock. Geophysical Research Letters, 43(22), 11-603.
939 Farquharson, J. I., Baud, P., & Heap, M. J. (2017). Inelastic compaction and permeability
940 evolution in volcanic rock. Solid Earth, 8(2), 561-581.
941 Fener, M., & Ince, I. (2015). Effects of the freeze–thaw (F–T) cycle on the andesitic rocks
942 (Sille-Konya/Turkey) used in construction building. Journal of African Earth Sciences,
943 109, 96-106.
944 Gonnermann, H. M. (2015). Magma fragmentation. Annual Review of Earth and Planetary
945 Sciences, 43, 431-458.
946 Griffiths, L., Heap, M. J., Xu, T., Chen, C.-f., & Baud, P. (2017). The influence of pore
947 geometry and orientation on the strength and stiffness of porous rock. Journal of
948 Structural Geology, 96, 149-160.
949 Graue, B., Siegesmund, S., & Middendorf, B. (2011). Quality assessment of replacement stones
950 for the Cologne Cathedral: mineralogical and petrophysical requirements. Environmental
951 Earth Sciences, 63(7-8), 1799-1822.

Gudmundsson, A. (1983a). Form and dimensions of dykes in eastern Iceland. Tectonophysics, 95(3-4), 295-307.
Gudmundsson, A. (1983b). Stress estimates from the length/width ratios of fractures. Journal of structural geology, 5(6), 623-626.
Gudmundsson, A. (1987). Formation and mechanics of magma reservoirs in Iceland. Geophysical Journal International, 91(1), 27-41.
Gudmundsson, A. (2006). How local stresses control magma-chamber ruptures, dyke injections, and eruptions in composite volcanoes. Earth-Science Reviews, 79(1-2), 1-31.
Gupta, A. S., & Rao, K. S. (2000). Weathering effects on the strength and deformational behaviour of crystalline rocks under uniaxial compression state. Engineering Geology, 56(3-4), 257-274.
Haimson, B. C., & Rummel, F. (1982). Hydrofracturing stress measurements in the Iceland research drilling project drill hole at Reydarfjordur, Iceland. Journal of Geophysical Research: Solid Earth, 87(B8), 6631-6649.
Harnett, C. E., Thomas, M. E., Purvance, M. D., & Neuberg, J. (2018). Using a discrete element approach to model lava dome emplacement and collapse. Journal of Volcanology and Geothermal Research, 359, 68-77.
Harnett, C. E., Kendrick, J. E., Lamur, A., Thomas, M. E., Stinton, A., Wallace, P. A., ... & Lavallée, Y. (2019). Evolution of mechanical properties of lava dome rocks across the 1995–2010 eruption of Soufrière Hills volcano, Montserrat. Frontiers in Earth Science, 7, 7.
Hashiba, K., & Fukui, K. (2015). Effect of water on the deformation and failure of rock in uniaxial tension. Rock Mechanics and Rock Engineering, 48(5), 1751-1761.
Heap, M. J., Lavallée, Y., Laumann, A., Hess, K. U., Meredith, P. G., & Dingwell, D. B. (2012). How tough is tuff in the event of fire? Geology, 40(4), 311-314.
Heap, M. J., Mollo, S., Vinciguerra, S., Lavallée, Y., Hess, K. U., Dingwell, D. B., ... & Iezzi, G. (2013). Thermal weakening of the carbonate basement under Mt. Etna volcano (Italy): implications for volcano instability. Journal of volcanology and geothermal research, 250, 42-60.
Heap, M. J., Xu, T., & Chen, C.-f. (2014a). The influence of porosity and vesicle size on the brittle strength of volcanic rocks and magma. Bulletin of Volcanology, 76(9), 1-15.
Heap, M. J., Baud, P., Meredith, P. G., Vinciguerra, S., & Reuschlé, T. (2014b). The permeability and elastic moduli of tuff from Campi Flegrei, Italy: implications for ground deformation modelling. Solid Earth, 5(1), 25-44.
Heap, M. J., Lavallée, Y., Petrakova, L., Baud, P., Reuschlé, T., Varley, N. R., & Dingwell, D. B. (2014c). Microstructural controls on the physical and mechanical properties of edifice-forming andesites at Volcán de Colima, Mexico. Journal of Geophysical Research: Solid Earth, 119(4), 2925-2963.
Heap, M. J., Xu, T., Kushnir, A. R., Kennedy, B. M., & Chen, C.-f. (2015a). Fracture of magma containing overpressurised pores. Journal of Volcanology and Geothermal Research, 301, 180-190.
Heap, M. J., Farquharson, J. I., Baud, P., Lavallée, Y., & Reuschlé, T. (2015b). Fracture and compaction of andesite in a volcanic edifice. Bulletin of volcanology, 77(6), 1-19.
Heap, M. J., Farquharson, J. I., Wadsworth, F. B., Kolzenburg, S., & Russell, J. K. (2015c). Timescales for permeability reduction and strength recovery in densifying magma. Earth and Planetary Science Letters, 429, 223-233.
Heap, M. J., Wadsworth, F. B., Xu, T., Chen, C.-f., & Tang, C.-a. (2016). The strength of heterogeneous volcanic rocks: a 2D approximation. Journal of Volcanology and Geothermal Research, 319, 1-11.

Heap, M., Kushnir, A., Griffiths, L., Wadsworth, F., Marmoni, G. M., Fiorucci, M., ... & Reuschlé, T. (2018). Fire resistance of the Mt. Epomeo Green Tuff, a widely-used building stone on Ischia Island (Italy). Volcanica, 1(1), 33-48.

Heap, M. J., Tuffen, H., Wadsworth, F. B., Reuschlé, T., Castro, J. M., & Schipper, C. I. (2019a). The permeability evolution of tuffisites and implications for outgassing through dense rhyolitic magma. Journal of Geophysical Research: Solid Earth, 124(8), 8281-8299.

Heap, M. J., Troll, V. R., Kushnir, A. R., Gilg, H. A., Collinson, A. S., Deegan, F. M., ... & Walter, T. R. (2019b). Hydrothermal alteration of andesitic lava domes can lead to explosive volcanic behaviour. Nature Communications, 10(1), 1-10.

Heap, M.J., and Violay, M.E.S. (2021). The mechanical behaviour and failure modes of volcanic rocks: a review. Bulletin of Volcanology, 83, 33 https://doi.org/10.1007/s00445-021-01447-2.

Heap M.J., Baumann, T., Gilg, H.A., Kolzenburg, S., Ryan, A., Villeneuve, M., Russell, J.K., Kennedy, L., Rosas-Carbajal, M., & Clynne M. (2021) Hydrothermal alteration can result in pore pressurization and volcano instability. Geology, 49, https://doi.org/10.1130/G49063.1.

Heiken, G., Wohletz, K., & Eichelberger, J. (1988). Fracture fillings and intrusive pyroclasts, Inyo Domes, California. Journal of Geophysical Research: Solid Earth, 93(B5), 4335-4350.

Hoek, E., & Brown, E. T. (2019). The Hoek–Brown failure criterion and GSI–2018 edition. Journal of Rock Mechanics and Geotechnical Engineering, 11(3), 445-463.

Holohan, E. P., Sudhaus, H., Walter, T. R., Schöpfer, M. P., & Walsh, J. J. (2017). Effects of host-rock fracturing on elastic-deformation source models of volcano deflation. Scientific reports, 7(1), 1-12.

Hornby, A. J., Lavallée, Y., Kendrick, J. E., De Angelis, S., Lamur, A., Lamb, O. D., ... & Chigna, G. (2019). Brittle-ductile deformation and tensile rupture of dome lava during inflation at Santiaguito, Guatemala. Journal of Geophysical Research: Solid Earth, 124(10), 10107-10131.

Ichihara, M., Rittel, D., & Sturtevant, B. (2002). Fragmentation of a porous viscoelastic material: Implications to magma fragmentation. Journal of Geophysical Research: Solid Earth, 107(B10), ECV-8.

Jónsson, S. (2012). Tensile rock mass strength estimated using InSAR. Geophysical Research Letters, 39(21).

Kahraman, S., & Yeken, T. (2010). Electrical resistivity measurement to predict uniaxial compressive and tensile strength of igneous rocks. Bulletin of Materials Science, 33(6), 731-735.

Karakuş, A., & Akatay, M. (2013). Determination of basic physical and mechanical properties of basaltic rocks from P-wave velocity. Nondestructive Testing and Evaluation, 28(4), 342-353.

Kendrick, J. E., Schaefer, L. N., Schauroth, J., Bell, A. F., Lamb, O. D., Lamur, A., ... & Kennedy, B. M. (2021). Physical and mechanical rock properties of a heterogeneous volcano: the case of Mount Unzen, Japan. Solid Earth, 12(3), 633-664.

Kılıç, A., & Teymen, A. (2008). Determination of mechanical properties of rocks using simple methods. Bulletin of Engineering Geology and the Environment, 67(2), 237.

Koyaguchi, T., Scheu, B., Mitani, N. K., & Melnik, O. (2008). A fragmentation criterion for highly viscous bubbly magmas estimated from shock tube experiments. Journal of Volcanology and Geothermal Research, 178(1), 58-71.

1049 Kremers, S., Scheu, B., Cordonnier, B., Spieler, O., & Dingwell, D. B. (2010). Influence of
1050 decompression rate on fragmentation processes: An experimental study. Journal of
1051 Volcanology and Geothermal Research, 193(3-4), 182-188.
1052 Kueppers, U., Scheu, B., Spieler, O., & Dingwell, D. B. (2006). Fragmentation efficiency of
1053 explosive volcanic eruptions: A study of experimentally generated pyroclasts. Journal of
1054 Volcanology and Geothermal Research, 153(1-2), 125-135.
1055 Kushnir, A. R., Martel, C., Champallier, R., & Arbaret, L. (2017). In situ confirmation of
1056 permeability development in shearing bubble-bearing melts and implications for volcanic
1057 outgassing. Earth and Planetary Science Letters, 458, 315-326.
1058 Laghaei, M., Baghbanan, A., Hashemolhosseini, H., & Dehghanipoodeh, M. (2018). Numerical
1059 determination of deformability and strength of 3D fractured rock mass. International
1060 Journal of Rock Mechanics and Mining Sciences, 110, 246-256.
1061 Lamb, O. D., De Angelis, S., Wall, R. J., Lamur, A., Varley, N. R., Reyes-Dávila, G., ... &
1062 Lavallée, Y. (2017). Seismic and experimental insights into eruption precursors at Volcán
1063 de Colima. Geophysical Research Letters, 44(12), 6092-6100.
1064 Lamur, A., Lavallée, Y., Iddon, F. E., Hornby, A. J., Kendrick, J. E., von Aulock, F. W., &
1065 Wadsworth, F. B. (2018). Disclosing the temperature of columnar jointing in lavas.
1066 Nature Communications, 9(1), 1-7.
1067 Lan, H., Chen, J., & Macciotta, R. (2019). Universal confined tensile strength of intact rock.
1068 Scientific Reports, 9(1), 1-9.
1069 Lavallée, Y., Varley, N. R., Alatorre-Ibargüengoitia, M. A., Hess, K. U., Kueppers, U., Mueller,
1070 S., ... & Dingwell, D. B. (2012). Magmatic architecture of dome-building eruptions at
1071 Volcán de Colima, Mexico. Bulletin of Volcanology, 74(1), 249-260.
1072 Li, J., Zhang, G., & Liu, M. (2019). Experimental investigation on the effect of confining
1073 pressure on the tensile strength of sandstone using hollow cylinder tensile test method.
1074 Arabian Journal of Geosciences, 12(24), 1-7.
1075 Malik, A., Chakraborty, T., Rao, K. S., & Kumar, D. (2017). Experiments to determine static
1076 and dynamic tensile strength of deccan trap rocks, India. Procedia Engineering, 191, 946-
1077 953.
1078 Manconi, A., Longpré, M. A., Walter, T. R., Troll, V. R., & Hansteen, T. H. (2009). The effects
1079 of flank collapses on volcano plumbing systems. Geology, 37(12), 1099-1102.
1080 Marmoni, G. M., Martino, S., Heap, M. J., & Reuschlé, T. (2017). Gravitational slope-
1081 deformation of a resurgent caldera: New insights from the mechanical behaviour of Mt.
1082 Nuovo tuffs (Ischia Island, Italy). Journal of Volcanology and Geothermal Research, 345,
1083 1-20.
1084 Martel, C., Dingwell, D. B., Spieler, O., Pichavant, M., & Wilke, M. (2000). Fragmentation of
1085 foamed silicic melts: an experimental study. Earth and Planetary Science Letters, 178(1-
1086 2), 47-58.
1087 Martel, C., Dingwell, D. B., Spieler, O., Pichavant, M., & Wilke, M. (2001). Experimental
1088 fragmentation of crystal-and vesicle-bearing silicic melts. Bulletin of Volcanology, 63(6),
1089 398-405.
1090 Mayer, K., Scheu, B., Gilg, H. A., Heap, M. J., Kennedy, B. M., Lavallée, Y., ... & Dingwell,
1091 D. B. (2015). Experimental constraints on phreatic eruption processes at Whakaari (White
1092 Island volcano). Journal of Volcanology and Geothermal Research, 302, 150-162.
1093 Mayer, K., Scheu, B., Montanaro, C., Yilmaz, T. I., Isaia, R., Aßbichler, D., & Dingwell, D. B.
1094 (2016). Hydrothermal alteration of surficial rocks at Solfatara (Campi Flegrei):
1095 Petrophysical properties and implications for phreatic eruption processes. Journal of
1096 Volcanology and Geothermal Research, 320, 128-143.
1097 McBirney, A. R., & Murase, T. (1970). Factors governing the formation of pyroclastic rocks.
1098 Bulletin Volcanologique, 34(2), 372-384.

Montanaro, C., Scheu, B., Mayer, K., Orsi, G., Moretti, R., Isaia, R., & Dingwell, D. B. (2016). Experimental investigations on the explosivity of steam-driven eruptions: A case study of Solfatara volcano (Campi Flegrei). Journal of Geophysical Research: Solid Earth, 121(11), 7996-8014.

Moon, K., & Yang, S. B. (2020). Cohesion and Internal Friction Angle Estimated from Brazilian Tensile Strength and Unconfined Compressive Strength of Volcanic Rocks in Jeju Island. Journal of the Korean Geotechnical Society, 36(2), 17-28.

Mueller, S., Melnik, O., Spieler, O., Scheu, B., & Dingwell, D. B. (2005). Permeability and degassing of dome lavas undergoing rapid decompression: an experimental determination. Bulletin of Volcanology, 67(6), 526-538.

Mueller, S., Scheu, B., Spieler, O., & Dingwell, D. B. (2008). Permeability control on magma fragmentation. Geology, 36(5), 399-402.

Nara, Y., Hiroyoshi, N., Yoneda, T., & Kaneko, K. (2010a). Effects of relative humidity and temperature on subcritical crack growth in igneous rock. International Journal of Rock Mechanics and Mining Sciences, 47(4), 640-646.

Nara, Y., Takada, M., Mori, D., Owada, H., Yoneda, T., & Kaneko, K. (2010b). Subcritical crack growth and long-term strength in rock and cementitious material. International Journal of Fracture, 164(1), 57-71.

Perras, M. A., & Diederichs, M. S. (2014). A review of the tensile strength of rock: concepts and testing. Geotechnical and Geological Engineering, 32(2), 525-546.

Richard, D., Scheu, B., Mueller, S. P., Spieler, O., & Dingwell, D. B. (2013). Outgassing: Influence on speed of magma fragmentation. Journal of Geophysical Research: Solid Earth, 118(3), 862-877.

Rinne, H. (2008). The Weibull distribution: a handbook. CRC press.

Ryan, A. G., Heap, M. J., Russell, J. K., Kennedy, L. A., & Clynne, M. A. (2020). Cyclic shear zone cataclasis and sintering during lava dome extrusion: Insights from Chaos Crags, Lassen Volcanic Center (USA). Journal of Volcanology and Geothermal Research, 401, 106935.

Sammis, C. G., & Ashby, M. F. (1986). The failure of brittle porous solids under compressive stress states. Acta Metallurgica, 34(3), 511-526.

Scheu, B., Spieler, O., & Dingwell, D. B. (2006). Dynamics of explosive volcanism at Unzen volcano: an experimental contribution. Bulletin of Volcanology, 69(2), 175-187.

Schultz, R. (1995). Limits on strength and deformation properties of jointed basaltic rock masses. Rock Mechanics and Rock Engineering, 28(1), 1-15.

Shea, T., Houghton, B. F., Gurioli, L., Cashman, K. V., Hammer, J. E., & Hobden, B. J. (2010). Textural studies of vesicles in volcanic rocks: an integrated methodology. Journal of Volcanology and Geothermal Research, 190(3-4), 271-289.

Siratovich, P. A., von Aulock, F. W., Lavallée, Y., Cole, J. W., Kennedy, B. M., & Villeneuve, M. C. (2015). Thermoelastic properties of the Rotokawa Andesite: a geothermal reservoir constraint. Journal of Volcanology and Geothermal Research, 301, 1-13.

Spieler, O., Kennedy, B., Kueppers, U., Dingwell, D. B., Scheu, B., & Taddeucci, J. (2004). The fragmentation threshold of pyroclastic rocks. Earth and Planetary Science Letters, 226(1-2), 139-148.

Tang, C.-a. (1997). Numerical simulation of progressive rock failure and associated seismicity. International Journal of Rock Mechanics and Mining Sciences, 34(2), 249-261.

Tang, C.-a., Liu, H., Lee, P. K. K., Tsui, Y., & Tham, L. (2000). Numerical studies of the influence of microstructure on rock failure in uniaxial compression—part I: effect of heterogeneity. International Journal of Rock Mechanics and Mining Sciences, 37(4), 555-569.

Tang, C.-a. & Tang, S. (2011). Applications of rock failure process analysis (RFPA) method. Journal of Rock Mechanics and Geotechnical Engineering, 3(4), 352-372.
Tang, C.-a. & Tang, S. (2020). Applications of Rock Failure Process Analysis (RFPA) to Rock Engineering. In Modelling Rock Fracturing Processes (pp. 421-459). Springer, Cham.
Troll, V. R., Hilton, D. R., Jolis, E. M., Chadwick, J. P., Blythe, L. S., Deegan, F. M., ... & Zimmer, M. (2012). Crustal CO2 liberation during the 2006 eruption and earthquake events at Merapi volcano, Indonesia. Geophysical Research Letters, 39(11).
Tuffen, H., Dingwell, D. B., & Pinkerton, H. (2003). Repeated fracture and healing of silicic magma generate flow banding and earthquakes? Geology, 31(12), 1089-1092.
Tuğrul, A., & Gürpinar, O. (1997). A proposed weathering classification for basalts and their engineering properties (Turkey). Bulletin of Engineering Geology and the Environment, 55(1), 139-149.
Ündül, Ö., & Er, S. (2017). Investigating the effects of micro-texture and geo-mechanical properties on the abrasiveness of volcanic rocks. Engineering Geology, 229, 85-94.
Varley, N., Connor, C. B., & Komorowski, J. C. (Eds.). (2019). Volcán de Colima: Portrait of a Persistently Hazardous Volcano. Springer.
Vasseur, J., Wadsworth, F. B., Lavallée, Y., Hess, K. U., & Dingwell, D. B. (2013). Volcanic sintering: timescales of viscous densification and strength recovery. Geophysical Research Letters, 40(21), 5658-5664.
Voltolini, M., Zandomeneghi, D., Mancini, L., & Polacci, M. (2011). Texture analysis of volcanic rock samples: quantitative study of crystals and vesicles shape preferred orientation from X-ray microtomography data. Journal of Volcanology and Geothermal Research, 202(1-2), 83-95.
Wadsworth, F. B., Witcher, T., Vossen, C. E., Hess, K. U., Unwin, H. E., Scheu, B., ... & Dingwell, D. B. (2018). Combined effusive-explosive silicic volcanism straddles the multiphase viscous-to-brittle transition. Nature Communications, 9(1), 1-8.
Walter, T. R., Harnett, C. E., Varley, N., Bracamontes, D. V., Salzer, J., Zorn, E. U., ... & Thomas, M. E. (2019). Imaging the 2013 explosive crater excavation and new dome formation at Volcán de Colima with TerraSAR-X, time-lapse cameras and modelling. Journal of Volcanology and Geothermal Research, 369, 224-237.
Wedekind, W., López-Doncel, R., Dohrmann, R., Kocher, M., & Siegesmund, S. (2013). Weathering of volcanic tuff rocks caused by moisture expansion. Environmental Earth Sciences, 69(4), 1203-1224.
Wiebe, R. A., Kolzenburg, S., Rooyakkers, S. M., & Stix, J. (2021). Plutonic record of a caldera-forming silicic eruption: The shatter zone of the Cadillac Mountain granite, coastal Maine. Geosphere, 17(1), 1-22.
Wiesmaier, S., Heap, M. J., Branca, S., Gilg, H. A., Kueppers, U., Hess, K. U., ... & Dingwell, D. B. (2015). Variability in composition and physical properties of the sedimentary basement of Mt Etna, Italy. Journal of volcanology and geothermal research, 302, 102-116.
Wright, H. M., Cashman, K. V., Gottesfeld, E. H., & Roberts, J. J. (2009). Pore structure of volcanic clasts: Measurements of permeability and electrical conductivity. Earth and Planetary Science Letters, 280(1-4), 93-104.
Wu, B., Yao, W., & Xia, K. (2016). An experimental study of dynamic tensile failure of rocks subjected to hydrostatic confinement. Rock Mechanics and Rock Engineering, 49(10), 3855-3864.
Xu, T., Tang, C.-a., Zhao, J., Li, L., & Heap, M. J. (2012). Modelling the time-dependent rheological behaviour of heterogeneous brittle rocks. Geophysical Journal International, 189(3), 1781-1796.

Yasar, S., & Komurlu, E. (2020). Water saturation induced changer in the indirect (Brazilian) tensile strength and the failure mode of some igneous rock materials. Geoscience Engineering, 66, 60-68.

Yavuz, A. B., Kaputoglu, S. A., Çolak, M., & Tanyu, B. F. (2017). Durability assessments of rare green andesites widely used as building stones in Buca (Izmir), Turkey. Environmental earth sciences, 76(5), 211.

Yuan, Y., Xu, T., Heap, M. J., Meredith, P. G., Yang, T., & Zhou, G. (2021). A three-dimensional mesoscale model for progressive time-dependent deformation and fracturing of brittle rock with application to slope stability. Computers and Geotechnics, 135, 104160.

Zhan, Y., & Gregg, P. M. (2019). How accurately can we model magma reservoir failure with uncertainties in host rock rheology? Journal of Geophysical Research: Solid Earth, 124(8), 8030-8042.

Zhang, Y. (1999). A criterion for the fragmentation of bubbly magma based on brittle failure theory. Nature, 402(6762), 648-650.

Zhou, G. L., Xu, T., Heap, M. J., Meredith, P. G., Mitchell, T. M., Sesnic, A. S. Y., & Yuan, Y. (2020). A three-dimensional numerical meso-approach to modeling time-independent deformation and fracturing of brittle rocks. Computers and Geotechnics, 117, 103274.

Zhu, W. C., & Tang, C.-a. (2006). Numerical simulation of Brazilian disk rock failure under static and dynamic loading. International Journal of Rock Mechanics and Mining Sciences, 43(2), 236-252.

Zhu, W. C., Bai, Y., Li, X. B., & Niu, L. L. (2012). Numerical simulation on rock failure under combined static and dynamic loading during SHPB tests. International Journal of Impact Engineering, 49, 142-157.

Zhu, W., Baud, P., Vinciguerra, S., & Wong, T. F. (2011). Micromechanics of brittle faulting and cataclastic flow in Alban Hills tuff. Journal of Geophysical Research: Solid Earth, 116(B6).

Zhu, W., Baud, P., Vinciguerra, S., & Wong, T. F. (2016). Micromechanics of brittle faulting and cataclastic flow in Mount Etna basalt. Journal of Geophysical Research: Solid Earth, 121(6), 4268-4289.

Zorn, E. U., Rowe, M. C., Cronin, S. J., Ryan, A. G., Kennedy, L. A., & Russell, J. K. (2018). Influence of porosity and groundmass crystallinity on dome rock strength: a case study from Mt. Taranaki, New Zealand. Bulletin of Volcanology, 80(4), 35.